applied sciences

MDPI

Article

A Complete Control-Oriented Model for Hydrogen Hybrid Renewable Microgrids with High-Voltage DC Bus Stabilized by Batteries and Supercapacitors

José Manuel Andújar Márquez *, Francisco José Vivas Fernández and Francisca Segura Manzano

Research Centre on Technology, Energy and Sustainability (CITES), University of Huelva, 21007 Huelva, Spain; francisco.vivas@diesia.uhu.es (F.J.V.F.); francisca.segura@diesia.uhu.es (F.S.M.)
* Correspondence: andujar@uhu.es

Abstract

The growing penetration of renewable energy sources requires resilient microgrids capable of providing stable and continuous operation. Hybrid energy storage systems (HESS), which integrate hydrogen-based storage systems (HBSS), battery storage systems (BSS), and supercapacitor banks (SCB), are essential to ensuring the flexibility and robustness of these microgrids. Accurate modelling of these microgrids is crucial for analysis, controller design, and performance optimization, but the complexity of HESS poses a significant challenge: simplified linear models fail to capture the inherent nonlinear dynamics, while nonlinear approaches often require excessive computational effort for real-time control applications. To address this challenge, this study presents a novel state space model with linear variable parameters (LPV), which effectively balances accuracy in capturing the nonlinear dynamics of the microgrid and computational efficiency. The research focuses on a high-voltage DC bus microgrid architecture, in which the BSS and SCB are connected directly in parallel to provide passive DC bus stabilization, a configuration that improves system resilience but has received limited attention in the existing literature. The proposed LPV framework employs recursive linearisation around variable operating points, generating a time-varying linear representation that accurately captures the nonlinear behaviour of the system. By relying exclusively on directly measurable state variables, the model eliminates the need for observers, facilitating its practical implementation. The developed model has been compared with a reference model validated in the literature, and the results have been excellent, with average errors, MAE, RAE and RMSE values remaining below 1.2% for all critical variables, including state-of-charge, DC bus voltage, and hydrogen level. At the same time, the model maintains remarkable computational efficiency, completing a 24-h simulation in just 1.49 s, more than twice as fast as its benchmark counterpart. This optimal combination of precision and efficiency makes the developed LPV model particularly suitable for advanced model-based control strategies, including real-time energy management systems (EMS) that use model predictive control (MPC). The developed model represents a significant advance in microgrid modelling, as it provides a general control-oriented approach that enables the design and operation of more resilient, efficient, and scalable renewable energy microgrids.

Keywords: state-space model; energy management system; renewable microgrids; hydrogen backup systems; supercapacitors; lead-acid battery; lithium-ion battery

check for updates

Academic Editors: Emilio Gomez-Lazaro, Raquel Villena-Ruiz, César Berna-Escriche and Paula Bastida-Molina

Received: 21 August 2025
Revised: 28 September 2025
Accepted: 7 October 2025
Published: 8 October 2025

Citation: Andújar Márquez, J.M.; Vivas Fernández, F.J.; Segura Manzano, F. A Complete Control-Oriented Model for Hydrogen Hybrid Renewable Microgrids with High-Voltage DC Bus Stabilized by Batteries and Supercapacitors. *Appl. Sci.* **2025**, *15*, 10810. https://doi.org/10.3390/app151910810

Copyright: © 2025 by the authors. Licensee MDPI, Basel, Switzerland. This article is an open access article distributed under the terms and conditions of the Creative Commons Attribution (CC BY) license (https://creativecommons.org/licenses/by/4.0/).

1. Introduction

The global energy sector faces significant challenges stemming from geopolitical instability, climate change imperatives, and grid resilience requirements [1,2]. In this context, microgrids have emerged as a strategic solution. Defined as relatively small-scale, controllable energy systems that connect local generation units to proximate users, microgrids are a key form of distributed generation [3,4]. Their current configurations predominantly incorporate local renewable energy sources, such as solar and wind power, thereby reducing dependence on fossil fuels and improving energy security [3,5]. Climate-focused policies, including the Grand Deal framework, further underscore their importance in facilitating decarbonisation and improving energy accessibility. The autonomous and secure operation of these systems is crucial for ensuring the resilience of critical infrastructure against disruptions from extreme weather or cyber threats [1,2]. Consequently, microgrids are established as fundamental components of sustainable energy systems, effectively combining climate mitigation with enhanced security and adaptability [5,6].

The evolution of microgrids points towards a broader paradigm: the development of a grid comprising hybrid microgrids for smart cities. Conceptually, this approach offers numerous advantages, such as superior power quality, reliability, security, and resiliency [7]. It also enables the integration of various energy carriers through energy hubs, allows for higher penetration of renewables with positive environmental impacts, facilitates self-healing as a key feature of smart grids, and can lead to reduced energy costs [7].

However, a primary challenge in renewable-based systems is the inherent climate dependency of sources like solar and wind, which results in stochastic generation patterns that preclude a guaranteed continuous electricity supply [3,8]. To address the resulting discrepancies between generation and consumption profiles, Energy Storage Systems (ESSs) are essential [3,8]. There is a wide range of technologies available to implement them, including battery banks (BBs), supercapacitor banks (SCBs), superconducting magnetic energy storage, flywheels, compressed air systems, and hydrogen-based solutions, each with distinct advantages and limitations [9]. Research demonstrates that Hybrid Energy Storage Systems (HESS), which integrate multiple technologies to operate synergistically, can effectively mitigate individual shortcomings while optimizing overall system performance [10,11].

For effective integration, renewable microgrids with HESS can be configured around DC buses, AC buses, or hybrid AC/DC architectures [11,12]. The configuration chosen to connect the components, either directly or through power converters, is critical, as it significantly influences both the complexity and controllability of individual elements and the microgrid as a whole [12,13].

At small to medium scales, there is growing consensus favouring DC bus-based microgrid architectures incorporating HESS configurations with BBs/SCBs and hydrogen as an energy vector [3,10]. This trend reflects increasing adoption of sophisticated hybrid systems integrating diverse components (batteries, supercapacitors, electrolysers, fuel cells (FCs), etc.) and technologies (lead-acid and Li-ion batteries, polymer electrolyte membrane (PEM) and high-temperature FCs, alkaline and PEM electrolysers, etc.), resulting in more complex system architectures and control requirements [8,11]. Figure 1 illustrates a representative configuration featuring comprehensive HESS integration with multiple degrees of freedom, which serves as the foundation for this investigation.

DC bus architectures provide notable advantages for microgrid integration, particularly in terms of control efficiency, as they facilitate direct generator and HESS connections while eliminating reactive power and frequency regulation challenges inherent to AC systems [3,14]. However, when AC buses (230 V single-phase or 400 V three-phase) derive from a primary DC bus, implementation of a high-voltage DC (HVDC) bus becomes necessary to maintain appropriate voltage ranges (see Figure 1). Proper integration and

control of microgrid components connected to the DC bus requires carefully selected power conditioner topologies tailored to the characteristics of each system (see Figure 1).

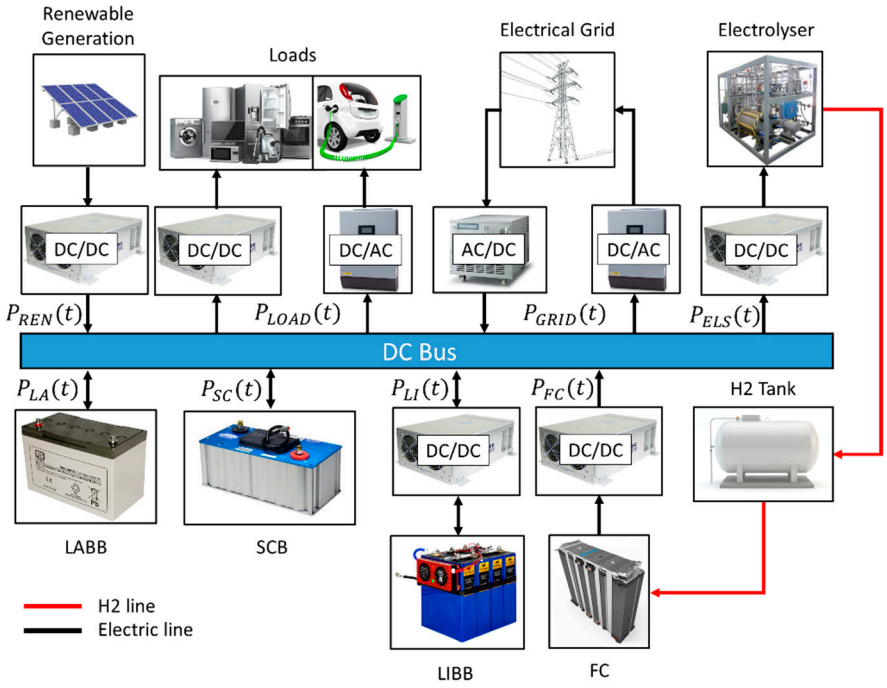

Figure 1. Microgrid Architecture.

Maintaining DC bus voltage stability is paramount for ensuring proper integration and operation of all microgrid components [14,15]. In configurations where power conditioners interface all elements with the DC bus, implementation of specialized control laws is required to maintain voltage stability [16]. The complexity of this control challenge escalates with system complexity, becoming particularly demanding in sophisticated architectures such as that depicted in Figure 1 [8,9]. Consequently, researchers have proposed DC bus architectures directly stabilized by BBs and/or SCBs, capitalizing on their dynamic response characteristics and voltage regulation capabilities [14,17]. Among various direct-connection topologies, the passive parallel BB/SCB configuration (Figure 1) offers superior performance in terms of efficiency, cost-effectiveness, control simplicity, dynamic response, voltage stability, and battery longevity by mitigating the harmful effects of high current peaks [18,19]. This architecture is particularly beneficial because demand spikes can stress and degrade the battery [20,21], while the supercapacitor's natural ability to absorb high-frequency current transients helps protect the battery, enhancing system robustness and extending its lifespan.

Notwithstanding these advantages, ensuring safe DC bus voltage operating ranges and extending component lifespans (both heavily dependent on operating conditions) requires precise control of BB/SCB charge/discharge dynamics and accurate bus voltage behaviour prediction [14,22]. The parallel topology complicates this task, as power distribution and dynamic responses depend on each element's internal impedance characteristics, which are not known a priori [18,23]. This challenge is further compounded by integration of additional system components such as supplementary battery systems, hydrogen-based storage systems (HBSS), and main electricity grid (MEG) connections, which collectively increase system degrees of freedom and overall complexity (see Figure 1).

These considerations clearly demonstrate the necessity for advanced multi-objective energy management systems (EMSs) in such complex architectures. Effective EMS implementation must optimize synergy among all system components to simultaneously ensure

both power balance (including temporal energy equilibrium) and DC bus voltage stability [3,24]. Model predictive control (MPC)-based EMS implementations currently represent the most promising solution [24,25], though they require development of microgrid models that optimally balance accuracy and computational efficiency. While non-model-based EMS approaches exist in literature [26–28], their inability to support analytical stability assessment or optimization represents a significant limitation.

1.1. Literature Review

The literature provides a wide range of contributions addressing the modelling of renewable microgrids with HESS and DC buses, each targeting different levels of architectural complexity and EMS.

A first category relies on nonlinear models of microgrid components to capture device-level dynamics with high fidelity. Representative works include [29–33], which analyse HESS-based microgrids in detail. Specifically, refs. [29–31] propose active BSS–SCB HESS architectures that use nonlinear equivalent circuit models based on Thévenin's theorem, including series resistance, parameter-dependent Thévenin voltage source, and SOC dynamics. Similarly, refs. [32,33] adopt nonlinear formulations for the optimal management of HBSS-based microgrids, where the electrolyser and fuel cell are modelled through nonlinear voltage–current characteristics governed by their internal electrochemical kinetics. While these approaches offer valuable information at the device level, their use in applications aimed at controlling entire microgrids is limited due to high computational cost, non-convex optimization, and difficulties in stability analysis [33,34]. Furthermore, the proposed nonlinear models often neglect system-level interactions, restricting their suitability for integrated microgrid studies. It should also be noted that all of the reviewed works consider active architectures, leaving passive configurations largely unexplored.

To overcome these challenges and take advantage of the benefits of linear control theory, numerous studies have developed linear or linearized models. These approaches maintain analytical tractability while capturing dominant system dynamics. The most common formulations are linear time-invariant (LTI) and piecewise-linear (PWL) models [35,36]. LTI models are based on constant matrices defined around nominal operating points of the system, whereas PWL models approximate nonlinear behaviours by dividing the state space into linear regions. Their use range from real-time controller design to supervisory EMS.

LTI models have been widely applied to simple active HESS architectures composed of BSS and SCB. Some examples are [37–40], where refs. [37,38] use the SOC of BSS and SCB as state variables for MPC-based EMS in DC microgrids on board ships and in homes, respectively, and refs. [39,40] include as states variables element-level voltages and SOCs for advanced controller design in multi-input and series–parallel converters, with the aim of regulating the DC bus voltage and ensuring power balance. Passive architectures have also been studied in [19,41], where LTI models describe SOC dynamics but adopt static representations of bus voltage and component currents, thereby neglecting DC bus voltage dynamics.

More complex architectures integrate the HBSS with the BSS or SCB. Studies [42–45] report LTI-based models of active HBSS–BSS systems. LTI models with SOC and hydrogen level (HL) as state variables are proposed in [42,43] for the model-based control of isolated DC microgrids. An LTI model studied in [44] addresses optimal electrical and thermal management under uncertainty using AI techniques. A passive HBSS–BSS microgrid is modelled in [45] using an element-by-element LTI formulation, where SOC, HL, and DC bus voltage are considered as state variables for the economic optimization of a grid-connected domestic DC microgrid. PWL models are explored in [46,47], focusing on renewable-

based domestic microgrids. In [46], HBSS efficiency is updated through SOC-HL-based PWL approximations of its power–efficiency curve, while [47] applies PWL formulations to capture BSS degradation by updating nominal capacity according to cycle depth and effective discharge.

Architectures combining HBSS and SCB are presented in [48,49], where LTI models with SOC and HL as state variables are used for EMS for DC microgrids intended for power and hydrogen co-generation, commercialisation, and vehicle-to-home/home-to-vehicle (V2H/H2V) integration.

Other contributions [32,50–52] explore hybrid configurations that integrate HBSS, BSS, and SCB into active architectures. These studies primarily design local PID controllers for power balance and DC bus regulation but rely on element-level models rather than comprehensive system formulations. Finally, ref. [53] develops an MPC-based EMS for an isolated HESS microgrid using a simplified LTI model with SOC and HL which, while practical, neglects DC bus voltage dynamics and limits applicability under real-world conditions.

In general, linear approaches such as LTI and PWL ensure tractability and compatibility with standard control methods, but they are constrained by working with constant parameters, which restricts accuracy under dynamic or long-term conditions

As an intermediate solution between purely nonlinear systems and LTI and PWL systems, linear models with parameter-varying emerge [54–56]. These preserve linear tractability while allowing system parameters to vary over time, thereby capturing nonlinear dynamics very effectively. For instance, ref. [54] proposes an LPV framework for a hybrid HESS with a passively connected LIBB and an actively connected SCB, modelled through equivalents based on Thévenin's theorem, with updates to the model parameters for SOC dynamics. Similarly, ref. [55] applies recursive linearization to fuel-cell dynamics in HBSS, and ref. [56] extends LPV methods to HBSS–LABB architectures in passive configurations. Despite their potential, LPV-based approaches remain scarce, particularly for complex systems combining HBSS, BSS, and SCB.

In summary, the literature highlights the need to reach a trade-off between model accuracy, computational efficiency, and applicability. Nonlinear models provide accuracy but entail high computational costs, while LTI and PWL models are efficient but limited in terms of dynamic coverage. Based on this, LPV-based approaches emerge as a promising solution, but they remain insufficiently explored for complex architectures integrating HBSS, BSS, and SCB.

1.2. Contributions

This study makes several significant contributions to the field of renewable microgrid modelling and control, addressing critical gaps identified in existing literature:

1. **Comprehensive Microgrid Architecture Modelling.** Presents a novel analysis and modelling framework for a practical renewable microgrid architecture featuring a complex hybrid energy storage system (HESS). The microgrid integrates different battery technologies, supercapacitors, and hydrogen-based storage, configured around a stabilised DC bus through the direct parallel connection of batteries and supercapacitors.
2. **General Formulation in State-Space.** Develops a complete, multivariable model in state-space that captures all the dynamics of interest for microgrid analysis and controller design. In fact, the model's behaviour over time is nonlinear, hence its accuracy. Furthermore, the model uses only measurable state variables, eliminating the need for state observers or estimators, while maintaining suitability for advanced model-based control strategies.
3. **Computationally Efficient LPV Approach.** The proposed model is formulated as a linear parameter variable (LPV) system, which ensures low computational cost (as

it is a linear model at each sampling time), while improving accuracy compared to traditional LTI models, since it addresses the nonlinearities of this type of microgrid through a recursive linearisation process around variable operating points. This means that although the model is linear in each sampling, it can be different, allowing the entire dynamics of the microgrid to be covered over time. Therefore, if the appropriate sampling times are chosen, the model captures nonlinearities, so that it behaves like non-linear model over time.

4. **Generalizable Modelling Methodology.** Development of a general and understandable modelling methodology that is easily applicable and extensible to different microgrids architectures.
5. **Comparative Advancements.** As summarized in Table 1, the proposed solution demonstrates clear improvements over existing approaches, as it simultaneously addresses four common limitations found in previous work published in the literature: greater complexity, interpretation and computational cost of non-linear models, over-simplified HESS architectures, omission of DC bus voltage dynamics, and reliance on static or linearized single-point models.

Table 1. Summary of solutions found in literature and authors' contribution.

	Microgrid Architecture					Model		
Reference	**BSS**	**SCB**	**HBSS**	**DC Bus Topology**	**BSS-SCB Architecture**	**DC Bus Voltage Model**	**Level of Integration**	**Type**
[29–31]	LIBB	Yes	No	Connection via power converters	Active	Yes	Element by element	Nonlinear Model
[32,33]	LIBB	Yes	Yes	Connection via power converters	Active	No	Element by element	Nonlinear & Static Model
[37,38]	LIBB	Yes	No	Connection via power converters	Active	No	Element by element	LTI
[39,40]	LIBB	Yes	No	Connection via power converters	Active	Yes	Element by element	LTI
[19,41]	LABB	Yes	No	Direct connection	Parallel-Passive	No	Element by element	LTI & Static Model
[42–44]	LIBB	No	Yes	Connection via power converters	Active	Yes	Element by element	LTI
[45]	LIBB	No	Yes	Direct connection	Passive	Yes	Element by element	LTI
[46,47]	LIBB	No	Yes	Connection via power converters	Active	No	Comprehensive microgrid model	PWL
[48,49]	No	Yes	Yes	Connection via power converters	Active	No	Comprehensive microgrid model	LTI
[32,50–52]	LABB or LIBB	Yes	Yes	Connection via power converters	Active	No	Element by element	LTI
[53]	LABB	Yes	Yes	Direct connection	Parallel-Passive	No	Comprehensive microgrid model	LTI
[54]	LIBB	Yes	No	Hybrid	Passive BSS Active SCB	No	Comprehensive microgrid model	LPV
[55]	No	No	Yes	Connection via power converters	-	No	Comprehensive microgrid model	LPV
[56]	LABB	No	Yes	Direct connection	-	Yes	Comprehensive microgrid model	LPV
Authors' approach	LABB and LIBB	Yes	Yes	Direct connection	Parallel-Passive	Yes	Comprehensive microgrid model	LPV

All these contributions, taken together, enable progress in the control of renewable microgrids, providing both theoretical foundations and practical tools for developing effective energy management systems (EMS) for complex HESS configurations. In particular, this work enables more accurate and reliable model-based control strategies to be implemented, which responds to a critical need in the field of complex renewable microgrids.

The rest of this article is organized as follows. Section 2 provides a detailed description of the architecture and operation of the microgrid under study. Section 3 develops its state-space model. Section 4 presents the results obtained using the developed model and compares it with a reference model from the literature. These results are analysed and discussed in Section 5. Finally, Section 6 outlines the main conclusions of the research.

2. Microgrid Architecture and Operation

The microgrid under study presented in Figure 1 is intended to be general and comprehensive, allowing interested researchers to adapt it to their specific cases. As illustrated, it is a complex renewable microgrid connected to the MEG. The EES comprises a LABB and a SCB, which directly support the DC bus via their direct connections. The EES is further complemented by a LIBB and a HBSS, each connected to the DC bus through their respective power conditioners. The sign criterion adopted is such that any power injected into the DC bus is considered negative and positive otherwise.

The microgrid of Figure 1 can be easily expanded from the DC bus by adding single-phase (230 V) and/or three-phase (400 V) AC buses through suitable DC/AC converters. However, as a major advantage for modelling purposes, all generation and load are referenced to the DC bus, so additional AC buses would simply be treated as another load or as interconnections with the MEG.

The operation of the microgrid, which is the basis of the model to be developed, assumes that renewable energy is not a control variable, i.e., all renewable energy is always harnessed through one or more of the following operations (performed by the corresponding EMS): powering loads, charging the SCB, charging the LABB, charging the LIBB, producing hydrogen, or selling electricity to the MEG.

Since the LABB and SCB are connected directly to the DC bus, their charging and discharging are not considered controlled variables. This direct connection leverages their complementary dynamics, a feature that would be compromised if they were connected through power converters [18]. In this case, the main function of the LABB is to stabilize the voltage on the DC bus, resulting in a narrow operating range determined by the established voltage limits. This differs from traditional BSSs usage, and therefore additional systems will be required to ensure a greater usable storage capacity of the HESS. The choice of lead-acid technology is justified by its lower cost and fewer charge/discharge management constraints compared to lithium-ion technology [57,58].

The SCB, operating in parallel with the LABB within a passive architecture, plays a critical role in attenuating sudden fluctuations in power demand or injection that could otherwise compromise the stability of the DC bus and the microgrid as a whole. It also mitigates the detrimental impact of such transients on the lifespan of the LABB [17].

The stabilization of the DC bus voltage by the LABB and the SCB simplifies the control laws of power conditioners connected to the DC bus, enabling them to focus solely on achieving maximum power transfer rather than stabilizing the voltage at their output.

For its part, LIBB serves as the main ESS operating in the short-term due to its superior efficiency and longer lifespan (characterized by a high number of cycles compared to the LABB).

On the other hand, the HESS operates as a long-term storage system, allowing hydrogen production, storage, and subsequent conversion back to electrical energy in a closed loop system.

As can be seen in Figure 1, power conditioners allow all elements to be integrated around the DC bus and manage power and energy flows effectively. Finally, the microgrid includes a bidirectional connection with the MEG, allowing for energy purchases and sales.

3. Microgrid Modelling Methodological Foundation Proposal

The following sections present the proposed mathematical analysis with the aim of developing a discrete linear state space model of the microgrid shown in Figure 1. As usual, the state variables correspond to those associated with energy storage systems (ESSs). The model is control-oriented and specifically formulated for energy management of the

microgrid. Consequently, aspects related to the degradation of the energy storage systems are not considered in this formulation.

3.1. Lead-Acid Battery and Supercapacitor Bank Model

To develop a model that balances accuracy with low computational cost, first-order Thévenin models have been selected for the modelling of the LABB and SCB, Figure 2. These models are well-established and have been previously validated in the scientific literature [59,60]. The reason for studying LABB and SCB together is that the two elements work in tandem, in a complementary manner, to stabilise the DC bus. Hybridizing batteries and supercapacitors in a parallel configuration enhances overall performance and simplifies the control of both systems. This is because the distribution of roles between them is entirely passive, governed by the internal dynamics of each component.

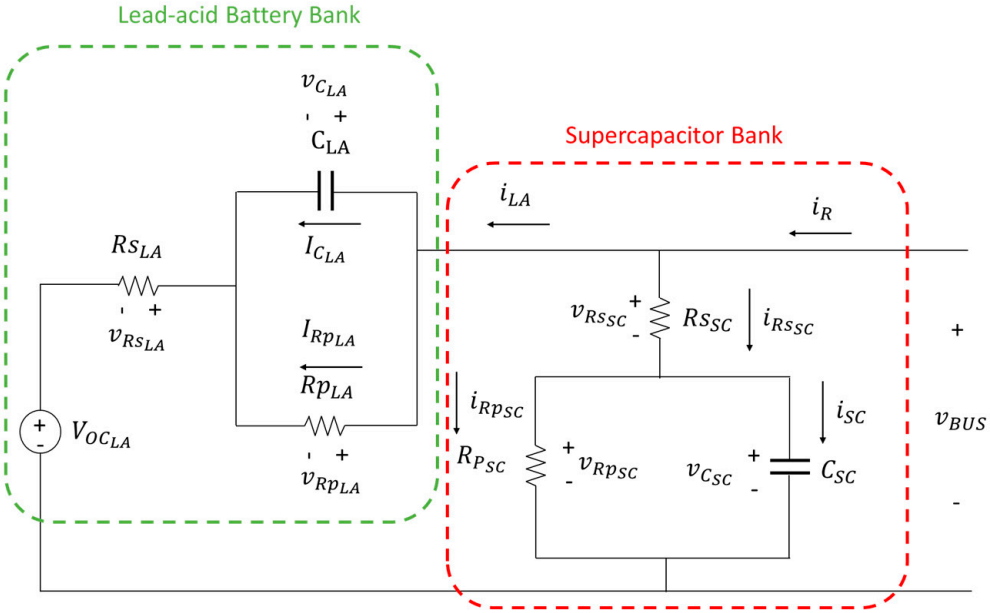

Figure 2. First-order Thévenin equivalent model for LABB and SCB.

By modelling the LABB as in Figure 2, the literature indicates that the Rs_{LA} and C_{LA} values can be considered practically constant with respect to SOC_{LA} in its useful working range: $SOC_{LA}(t) \in [30\%, 90\%]$, [61,62]. However, Rp_{LA} exhibits a strong nonlinear relationship with SOC_{LA}, [61,62]. Therefore, the following hypotheses are made (1).

$$\begin{gathered} Rs_{LA}(t) \approx R_{S_{LA}} \\ Rp_{LA}(t) = f_{Rp_{LA}}(SOC_{LA}(t)) \\ C_{LA}(t) \approx C_{LA} \end{gathered} \tag{1}$$

If Rs_{LA} and C_{LA} cannot be considered constant, the following mathematical analysis remains valid; only a dependency function for these parameters concerning SOC_{LA} would need to be included, similar to the approach for the Rp_{LA} parameter.

According to Kirchoff's current law (KCL), the LABB capacitor current ($i_{C_{LA}}(t)$) is calculated as in (2).

$$i_{C_{LA}}(t) = C_{LA}\frac{dv_{C_{LA}}(t)}{dt} = i_{LA}(t) - i_{Rp_{LA}}(t) \tag{2}$$

Defined $i_{Rp_{LA}}(t)$ in (3), $\frac{dv_{C_{LA}}(t)}{dt}$ is calculated in (4):

$$i_{Rp_{LA}}(t) = \frac{v_{C_{LA}}(t)}{Rp_{LA}} \tag{3}$$

$$\frac{dv_{C_{LA}}(t)}{dt} = i_{LA}(t)\frac{1}{C_{LA}} - v_{C_{LA}}(t)\frac{1}{Rp_{LA}\cdot C_{LA}} \tag{4}$$

Considering (1), (4) can be rewritten as (5):

$$\frac{dv_{C_{LA}}(t)}{dt} = i_{LA}(t)\frac{1}{C_{LA}} - v_{C_{LA}}(t)\frac{1}{f_{Rp}(SOC_{LA}(t))\cdot C_{LA}} \tag{5}$$

Applying Taylor's theorem to the nonlinear term in (5), $\frac{v_{C_{LA}}(t)}{f_{Rp_{LA}}(SOC_{LA}(t))}$, yields the approximation (6).

$$\frac{dv_{C_{LA}}(t)}{dt} = i_{LA}(t)\frac{1}{C_{LA}} - SOC_{LA}(t)\frac{A_{T_1}(k)}{C_{LA}} - v_{C_{LA}}(t)\frac{B_{T_1}(k)}{C_{LA}} - \frac{C_{T_1}(k)}{C_{LA}} \tag{6}$$

where

$$A_{T_1}(k) = \left.\frac{\partial f(x)}{\partial SOC_{LA}}\right|_{[SOC_{LA}(\overline{x}),\, v_{C_{LA}}(\overline{x})]}$$

$$B_{T_1}(k) = \left.\frac{\partial f(x)}{\partial v_{C_{LA}}}\right|_{[SOC_{LA}(\overline{x}),\, v_{C_{LA}}(\overline{x})]}$$

$$C_{T_1}(k) = f\big(SOC_{LA}(\overline{x}),\, v_{C_{LA}}(\overline{x})\big) - SOC_{LA}(\overline{x})\left.\frac{\partial f(x)}{\partial SOC_{LA}}\right|_{[SOC_{LA}(\overline{x}),\, v_{C_{LA}}(\overline{x})]} - v_{C_{LA}}(\overline{x})\left.\frac{\partial f(x)}{\partial v_{C_{LA}}}\right|_{[SOC_{LA}(\overline{x}),\, v_{C_{LA}}(\overline{x})]}$$

To improve the model's accuracy in the presence of strong nonlinearities and its computational efficiency, the linearization point in the recursive linearisation process will be defined using the values obtained in the previous sampling, $\overline{x} = \big[SOC_{LA}(k-1), v_{C_{LA}}(k-1)\big]$. Specifically, the proposed recursive linearisation approach separates offline and online tasks; the general Taylor series expressions are derived offline once, and during operation, the algorithm merely evaluates these precomputed functions using the parameters from the previous sampling. This process is highly efficient, as it only requires updating the model parameters with the precomputed derivative expressions, resulting in a very low and predictable computational cost per sampling period.

Again, according to KCL, the SCB capacitor current ($i_{SC}(t)$) is calculated as in (7).

$$i_{SC}(t) = C_{SC}\frac{dv_{C_{SC}}(t)}{dt} = i_{Rs_{SC}}(t) - i_{Rp_{SC}}(t) \tag{7}$$

For its part, $i_{Rs_{SC}}(t)$ can also be obtained from KCL, as shown in (8).

$$i_{Rs_{SC}}(t) = i_R(t) - i_{LA}(t) \tag{8}$$

Defined $i_{Rp_{SC}}(t)$ in (9), $\frac{dv_{C_{SC}}(t)}{dt}$ is calculated in (10):

$$i_{Rp_{SC}}(t) = \frac{v_{C_{SC}}(t)}{Rp_{SC}} \tag{9}$$

$$\frac{dv_{C_{SC}}(t)}{dt} = i_R(t)\frac{1}{C_{SC}} - i_{LA}(t)\frac{1}{C_{SC}} - v_{C_{SC}}(t)\frac{1}{Rp_{SC}\cdot C_{SC}} \tag{10}$$

To obtain a discrete model, (6) and (10) are discretized using the backward Euler method, resulting in (11) and (12), respectively.

$$v_{C_{LA}}(k+1) = v_{C_{LA}}(k)\left(1 - \frac{B_{T_1}(k)\cdot T}{C_{LA}}\right) + i_{LA}(k)\frac{T}{C_{LA}} - SOC_{LA}(k)\frac{A_{T_1}(k)\cdot T}{C_{LA}} - \frac{C_{T_1}\cdot T}{C_{LA}} \quad (11)$$

$$v_{C_{SC}}(k+1) = v_{C_{SC}}(k)\left(1 - \frac{T}{Rp_{SC}\cdot C_{SC}}\right) + i_R(k)\frac{T}{C_{SC}} - i_{LA}(k)\frac{T}{C_{SC}} \quad (12)$$

where T is the sampling time. To derive a state-space model, $i_{LA}(k)$ must be expressed as a function of the state variables. From Figure 2, (13) is obtained.

$$i_{LA}(k) = i_R(k) - i_{Rs_{SC}}(k) \quad (13)$$

where again from Figure 2, $i_{Rs_{SC}}(k)$ is given by (14).

$$i_{Rs_{SC}}(k) = v_{OC_{LA}}(k)\frac{1}{Rs_{SC}} + i_{LA}(k)\frac{Rs_{LA}}{Rs_{SC}} + v_{C_{LA}}(k)\frac{1}{Rs_{SC}} - v_{C_{SC}}(k)\frac{1}{Rs_{SC}} \quad (14)$$

Considering (14), (13) can be rewritten as (15):

$$i_{LA}(k) = i_R(k)\frac{Rs_{SC}}{Rs_{SC}+Rs_{LA}} - v_{OC_{LA}}(k)\frac{1}{Rs_{SC}+Rs_{LA}} - v_{C_{LA}}(k)\frac{1}{Rs_{SC}+Rs_{LA}} + v_{C_{SC}}(k)\frac{1}{Rs_{SC}+Rs_{LA}} \quad (15)$$

Considering the experimental behaviour of LABBs within the recommended operating region, a linear relationship between $V_{OC_{LA}}(k)$ and $SOC_{LA}(k)$ can be established, [63]. This allows to write (16).

$$v_{OC_{LA}}(k) = A_{LA}\cdot SOC_{LA}(k) + B_{LA} \quad (16)$$

From (16), (15) can be written as (17):

$$\begin{aligned} i_{LA}(k) = {} & i_R(k)\tfrac{Rs_{SC}}{Rs_{SC}+Rs_{LA}} - SOC_{LA}(k)\tfrac{A_{LA}}{Rs_{SC}+Rs_{LA}} - \tfrac{B_{LA}}{Rs_{SC}+Rs_{LA}} - v_{C_{LA}}(k)\tfrac{1}{Rs_{SC}+Rs_{LA}} + \\ & + v_{C_{SC}}(k)\tfrac{1}{Rs_{SC}+Rs_{LA}} \end{aligned} \quad (17)$$

Finally, by substituting (17) into (11) and (12), (18) and (19) are obtained, respectively, where the voltages in the LABB and SCB are expressed as functions of the state variables.

$$\begin{aligned} v_{C_{LA}}(k+1) = {} & v_{C_{LA}}(k)\left(1 - \tfrac{T}{C_{LA}}\left(B_{T_1}(k) + \tfrac{1}{Rs_{SC}+Rs_{LA}}\right)\right) + v_{C_{SC}}(k)\tfrac{T}{C_{LA}(Rs_{SC}+Rs_{LA})} - \\ & - SOC_{LA}(k)\left(\tfrac{T}{C_{LA}}\left(A_{T_1}(k) + \tfrac{A_{LA}}{Rs_{SC}+Rs_{LA}}\right)\right) + i_R(k)\tfrac{Rs_{SC}\cdot T}{C_{LA}(Rs_{SC}+Rs_{LA})} \\ & - \tfrac{T}{C_{LA}}\left(\tfrac{B_{LA}}{Rs_{SC}+Rs_{LA}} + C_{T_1}(k)\right) \end{aligned} \quad (18)$$

$$\begin{aligned} v_{C_{SC}}(k+1) = {} & v_{C_{LA}}(k)\tfrac{T}{C_{SC}(Rs_{SC}+Rs_{LA})} + v_{C_{SC}}(k)\left(1 - \tfrac{T}{C_{SC}}\left(\tfrac{1}{Rp_{SC}} + \tfrac{1}{Rs_{SC}+Rs_{LA}}\right)\right) + \\ & + SOC_{LA}(k)\tfrac{A_{LA}\cdot T}{C_{SC}(Rs_{SC}+Rs_{LA})} + i_R(k)\left(\tfrac{T}{C_{SC}}\left(1 - \tfrac{Rs_{SC}}{Rs_{SC}+Rs_{LA}}\right)\right) \\ & + \tfrac{B_{LA}\cdot T}{C_{SC}(Rs_{SC}+Rs_{LA})} \end{aligned} \quad (19)$$

3.1.1. LABB State of Charge Model

The $SOC_{LA}(k)$ of the LABB is estimated from the charge/discharge efficiency multiplied by the number of Ah of charge/discharge with respect to its nominal capacity, according to the Coulomb counting method [64]. This is expressed in (20).

$$SOC_{LA}(t) = SOC_{LA}(t_0) + \frac{\eta_{LA}(t)}{C_{N_{LA}}(t)}\int_{t_0}^{t} i_{LA}(t)\,dt \quad (20)$$

To obtain a discrete model, (20) is discretized using the backward Euler method considering $T = t - t_0$, i.e., (21).

$$SOC_{LA}(k+1) = SOC_{LA}(k) + i_{LA}(k)\frac{\eta_{LA}(k)\cdot T}{C_{N_{LA}}(k)} \tag{21}$$

From (17), (21) can be written as (22).

$$\begin{aligned} SOC_{LA}\ (k+1) = &-v_{C_{LA}}(k)\frac{\eta_{LA}(k)\cdot T}{C_{N_{LA}}(k)(Rs_{SC}+Rs_{LA})} + v_{C_{SC}}(k)\frac{\eta_{LA}(k)\cdot T}{C_{N_{LA}}(k)(Rs_{SC}+Rs_{LA})} + \\ &+SOC_{LA}\ (k)\left(1 - \frac{\eta_{LA}(k)\cdot A_{LA}\cdot T}{C_{N_{LA}}(k)(Rs_{SC}+Rs_{LA})}\right) + i_R(k)\frac{\eta_{LA}(k)\cdot Rs_{SC}\cdot T}{C_{N_{LA}}(k)(Rs_{SC}+Rs_{LA})} \\ &- \frac{\eta_{LA}(k)\cdot B_{LA}\cdot T}{C_{N_{LA}}(k)(Rs_{SC}+Rs_{LA})} \end{aligned} \tag{22}$$

To consider the non-idealities of the system and improve the accuracy of the model, it has been considered that the parameters $\eta_{LA}(k)$ and $C_{N_{LA}}(k)$ can vary in each sampling period, depending on degradation and operating conditions. The expressions modelled and validated in [64] can be used for their calculation.

3.1.2. VDC Bus Model

Applying the Kirchoff's voltage law (KLV) from Figure 2, the LABB voltage and, therefore, the DC bus voltage, can be expressed according to (23).

$$v_{BUS}(k) = v_{OC_{LA}}(k) + i_{LA}(k)\cdot Rs_{LA} + v_{C_{LA}}(k) \tag{23}$$

By inserting (16) and (17) into (23), (24) can be obtained.

$$\begin{aligned} v_{BUS}(k) = &\ v_{C_{LA}}(k)\left(1 - \frac{Rs_{LA}}{Rs_{SC}+Rs_{LA}}\right) + v_{C_{SC}}(k)\frac{Rs_{LA}}{Rs_{SC}+Rs_{LA}} + SOC_{LA}\ (k) \\ &\cdot A_{LA}\left(1 - \frac{Rs_{LA}}{Rs_{SC}+Rs_{LA}}\right) + i_R(k)\frac{Rs_{LA}\cdot Rs_{SC}}{Rs_{SC}+Rs_{LA}} + B_{LA}\left(1 - \frac{Rs_{LA}}{Rs_{SC}+Rs_{LA}}\right) \end{aligned} \tag{24}$$

3.2. Lithium-Ion Battery Model

3.2.1. Battery Voltage Model

As with the LABB and SCB, the widely known first-order Thévenin model will be used to model the LIBB [65,66], as shown in Figure 3.

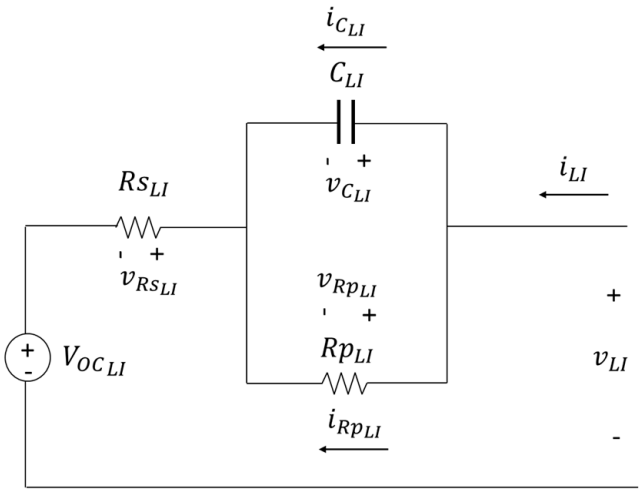

Figure 3. First-order Thévenin equivalent model for LIBB.

When modelling the LIBB as in Figure 3, the literature indicates that, similarly to the LABB, the Rs_{LI} and C_{LI} values can be considered practically constant with respect to SOC_{LI} in its useful working range: $SOC_{LI}(t) \in [30\%, 90\%]$, [65,67]. However, Rp_{LI} exhibits a strong nonlinear relationship with SOC_{LI} [65,67]. Based on the above, the parameters of LIBB can be expressed as in (25).

$$\begin{gathered} Rs_{LI}(t) \approx R_{S_{LI}} \\ Rp_{LI}(t) = f_{Rp_{LI}}(SOC_{LI}(t)) \\ C_{LI}(t) \approx C_{LI} \end{gathered} \tag{25}$$

Once again, if Rs_{LI} and C_{LI} cannot be considered constant, the following mathematical analysis remains valid, as it would only be necessary to take into account a dependency function for these parameters in relation to SOC_{LI}, similar to the approach used for the Rp_{LI} parameter.

According to KCL, the LIBB capacitor current ($i_{C_{LI}}(t)$) is calculated as in (26).

$$i_{C_{LI}}(t) = C_{LI}\frac{dv_{C_{LI}}(t)}{dt} = i_{LI}(t) - i_{Rp_{LI}}(t) \tag{26}$$

Defined $i_{Rp_{LI}}(t)$ in (27), $\frac{dv_{C_{LI}}(t)}{dt}$ is calculated in (28):

$$i_{Rp_{LI}}(t) = \frac{v_{C_{LI}}(t)}{Rp_{LI}} \tag{27}$$

$$\frac{dv_{C_{LI}}(t)}{dt} = i_{LI}(t)\frac{1}{C_{LI}} - v_{C_{LI}}(t)\frac{1}{Rp_{LI}\cdot C_{LI}} \tag{28}$$

From (25), (28) can be rewritten as (29):

$$\frac{dv_{C_{LI}}(t)}{dt} = i_{LI}(t)\frac{1}{C_{LI}} - v_{C_{LI}}(t)\frac{1}{f_{Rp_{LI}}(SOC_{LI}(t))\cdot C_{LI}} \tag{29}$$

As was done from (5) to (6), applying Taylor's theorem to the nonlinear term in (29), $\frac{v_{C_{LI}}(t)}{f_{Rp_{LI}}(SOC_{LI}(t))}$, yields the approximation (30).

$$\frac{dv_{C_{LI}}(t)}{dt} = i_{LI}(t)\frac{1}{C_{LI}} - SOC_{LI}(t)\frac{A_{T_2}(k)}{C_{LI}} - v_{C_{LI}}(t)\frac{B_{T_2}(k)}{C_{LI}} - \frac{C_{T_2}(k)}{C_{LI}} \tag{30}$$

where

$$A_{T_2}(k) = \left.\frac{\partial f(x)}{\partial SOC_{LI}}\right|_{[SOC_{LI}(\overline{x}),\, v_{C_{LI}}(\overline{x})]}$$

$$B_{T_2}(k) = \left.\frac{\partial f(x)}{\partial v_{C_{LI}}}\right|_{[SOC_{LI}(\overline{x}),\, v_{C_{LI}}(\overline{x})]}$$

$$C_{T_2}(k) = f\left(SOC_{LI}(\overline{x}),\, v_{C_{LI}}(\overline{x})\right) - SOC_{LI}(\overline{x})\left.\frac{\partial f(x)}{\partial SOC_{LI}}\right|_{[SOC_{LI}(\overline{x}),\, v_{C_{LI}}(\overline{x})]} - v_{C_{LI}}(\overline{x})\left.\frac{\partial f(x)}{\partial v_{C_{LI}}}\right|_{[SOC_{LI}(\overline{x}),\, v_{C_{LI}}(\overline{x})]}$$

Once again, to improve model accuracy in the presence of strong nonlinearities, the linearisation point in the recursive linearisation process will be done using the values obtained in the previous sampling, $\overline{x} = \left[SOC_{LI}(k-1), v_{C_{LI}}(k-1)\right]$. Again, this process is highly computationally efficient, as it only involves updating model parameters using precomputed derivative expressions.

To obtain a discrete model, (30) is discretized using the backward Euler method, Thus, (31) is obtained.

$$v_{C_{LI}}(k+1) = v_{C_{LI}}(k)\left(1 - \frac{B_{T_2}(k)\cdot T}{C_{LI}}\right) + i_{LI}(k)\frac{T}{C_{LI}} - SOC_{LI}(k)\frac{A_{T_2}(k)\cdot T}{C_{LI}} - \frac{C_{T_2}(k)\cdot T}{C_{LI}} \quad (31)$$

Applying the KVL in Figure 3, the LIBB voltage can be expressed according to (32).

$$v_{LI}(k) = v_{OC_{LI}}(k) + i_{LI}(k)\cdot Rs_{LI} + v_{C_{LI}}(k) \quad (32)$$

Finally, considering the experimental behaviour of LIBBs within the recommended operating region, a linear relationship between $V_{OC_{LI}}(k)$ and $SOC_{LI}(k)$ can be established [63]. This allows to write (33).

$$v_{OC_{LI}}(k) = A_{LI}\cdot SOC_{LI}(k) + B_{LI} \quad (33)$$

From (33), (32) can be written now as (34).

$$v_{LI}(k) = A_{LI}\cdot SOC_{LI}(k) + B_{LI} + i_{LI}(k)\cdot Rs_{LI} + v_{C_{LI}}(k) \quad (34)$$

3.2.2. LIBB State of Charge Model

The $SOC_{LI}(k)$ of the LIBB can be calculated as in the case of LABB. This allows obtaining (35).

$$SOC_{LI}(t) = SOC_{LI}(t_0) + \frac{\eta_{LI}(t)}{C_{N_{LI}}(t)}\int_{t_0}^{t} i_{LI}(t)\,dt \quad (35)$$

To obtain a discrete model, (35) is discretised using the backward Euler method, resulting in (36).

$$SOC_{LI}(k+1) = SOC_{LI}(k) + i_{LI}(k)\frac{\eta_{LI}(k)\cdot T}{C_{N_{LI}}(k)} \quad (36)$$

Analogous to LABB, it has been considered that the parameters $\eta_{LI}(k)$ and $C_{N_{LI}}(k)$ may vary in each sampling period, depending on the characteristic parameters of the battery, accumulated degradation, etc. The expressions modelled and validated in [64] can be used for their calculation.

3.3. Hydrogen Storage System Model

The hydrogen level is defined by a mass balance, considering its production and consumption by the electrolyser and the FC, respectively [68,69]. This is expressed by (37).

$$H_L(t) = H_L(t_0) + \int_{t_0}^{t}(i_{ELS}(t)\cdot r_{ELS} - i_{FC}(t)\cdot r_{FC})dt \quad (37)$$

The values of r_{ELS} and r_{FC}, are constant and depend on the characteristics of each equipment according to Faraday's Law [64,70], which makes the model general and applicable to all electrolyser and fuel cell technologies. Thus, in (38), r_x is the electrolyser hydrogen production ratio (x = *ELS*) or FC hydrogen consumption ratio (x = *FC*) in Nm^3/A. Similarly, N_x is the number of cells of the electrolyser (x = *ELS*) or FC stack (x = *FC*).

$$r_x = \frac{N_x\cdot M_{H_2}}{z\cdot F\cdot \rho_{H_2}} \quad (38)$$

As usual in this research, to obtain a discrete model, (38) is discretised using the backward Euler method. This allows to obtain (39).

$$H_L(k+1) = H_L(k) + i_{H_2}(k) \cdot r_{H_2}(k) \cdot T \tag{39}$$

It will be assumed that, as usual, the electrolyser and FC do not operate simultaneously. Thus, $i_{H_2}(k)$ and $r_{H_2}(k)$ will be $i_{ELS}(k)$ or $i_{FC}(k)$, and r_{ELS} or r_{FC} depending on whether the electrolyser or the FC is operating, respectively. Nevertheless, the model can be easily extended to consider the operation of both hydrogen elements separately. According to the mass balance in (37), the term $i_{H_2}(k) \cdot r_{H_2}(k) \cdot T$ (39) can be rewritten as $i_{H_2}(k) \cdot r_{H_2}(k) = i_{elec}(k) \cdot r_{elec}(k) \cdot T - i_{fc}(k) \cdot r_{fc}(k) \cdot T$.

3.4. Power Balance

Considering that the DC bus voltage is stabilized by the LABB and SCB set, for small sampling periods, the DC bus voltage can be considered constant, and therefore, the power control in the microgrid translates in practice into the implementation of a current control. Then, from Figure 1, the power balance on the DC bus can be rewritten as the current balance described in (40).

$$-i_{REN}(k) + i_{LOAD}(k) + i_{LA}(k) + i_{SC}(k) + i_{LI}(k) + i_{H_2}(k) + i_{GRID}(k) = 0 \tag{40}$$

The adopted sign criterion is that any power injected to the DC bus is considered negative and positive otherwise. Therefore, according to (40), the current demands will always be positive. The terms in each sampling associated with the operation of battery banks ($i_{LA}(k)$ and $i_{LI}(k)$) and the supercapacitor bank ($i_{SC}(k)$) will be positive or negative, depending on whether they are charging (drawing current from the DC bus) or discharging (injecting current to the DC bus), respectively. The HBSS current term ($i_{H2}(k)$) will be positive or negative, depending on whether the electrolyser (current demand from the bus) or the FC (current injection to the bus) is in operation, respectively. Similarly, in each sampling, the term associated with the MEG ($i_{GRID}(k)$) will be positive or negative, depending on whether the microgrid is supplying or demanding current from the MEG, respectively.

From Figure 2, $i_R(k) = i_{LA}(k) + i_{SC}(k)$. Then, defining $i_{BAL}(k) = -i_{REN}(k) + i_{LOAD}(k)$, (40) can be written as (41).

$$i_R(k) = -i_{BAL}(k) - i_{LI}(k) - i_{H_2}(k) - i_{GRID}(k) \tag{41}$$

Again, if simultaneous operation of the electrolyser and fuel cell is considered, $i_{H_2}(k)$ can be expressed as $i_{H_2}(k) = i_{elec}(k) - i_{fc}(k)$.

3.5. Discrete State-Space Model

Now, based on what has been developed, an LPV state-space model of the microgrid under study will be made as expressed in (42). For the representation of the matrices A, B, C, D, E, F, G and H, it must be considered that commas separate the elements within the same row, and semicolons separate the rows.

$$\begin{aligned} x(k+1) &= A \cdot x(k) + B \cdot u(k) + E \cdot w(k) + F \\ y(k) &= C \cdot x(k) + D \cdot u(k) + G \cdot w(k) + H \end{aligned} \tag{42}$$

where following (18), (19), (22), (31), (36) and (39) for the state equation; and (22), (24), (34), (36) and (39) for the output equation, (43) is obtained.

$$
\begin{aligned}
&(k) = \left[v_{C_{LA}}(k); v_{C_{SC}}(k); SOC_{LA}(k); v_{C_{LI}}(k); SOC_{LI}(k); H_L(k)\right]\\
&y(k) = \left[v_{BUS}(k); SOC_{LA}\ (k); v_{LI}(k); SOC_{LI}(k); H_L(k)\right]\\
&u(k) = \left[i_{LI}(k); i_{H_2}(k); i_{GRID}(k)\right]\\
&w(k) = \left[i_{BAL}(k)\right]\\
&A = \left[1 - \frac{T}{C_{LA}}\left(B_{T_1}(k) + \frac{1}{Rs_{SC}+Rs_{LA}}\right), \frac{T}{C_{LA}(Rs_{SC}+Rs_{LA})}, -\frac{T}{C_{LA}}\left(A_{T_1}(k) + \frac{A_{LA}}{Rs_{SC}+Rs_{LA}}\right), 0, 0, 0;\right.\\
&\frac{T}{C_{SC}(Rs_{SC}+Rs_{LA})}, 1 - \frac{T}{C_{SC}}\left(\frac{1}{Rp_{SC}} + \frac{1}{Rs_{SC}+Rs_{LA}}\right), \frac{A_{LA}\cdot T}{C_{SC}(Rs_{SC}+Rs_{LA})}, 0, 0, 0;\\
&-\frac{\eta_{LA}(k)\cdot T}{C_{N_{LA}}(k)(Rs_{SC}+Rs_{LA})}, \frac{\eta_{LA}(k)\cdot T}{C_{N_{LA}}(k)(Rs_{SC}+Rs_{LA})}, 1 - \frac{\eta_{LA}(k)\cdot A_{LA}\cdot T}{C_{N_{LA}}(k)(Rs_{SC}+Rs_{LA})},\ 0,\ 0,\ 0;\\
&\left.0, 0, 0, 1 - \frac{B_{T_2}(k)\cdot T}{C_{LI}}, -\frac{A_{T_2}(k)\cdot T}{C_{LI}}, 0;\ 0, 0, 0, 0, 1, 0; 0, 0, 0, 0, 0, 1\right]\\
&B = \left[-\frac{Rs_{SC}\cdot T}{C_{LA}(Rs_{SC}+Rs_{LA})}, -\frac{Rs_{SC}\cdot T}{C_{LA}(Rs_{SC}+Rs_{LA})}, -\frac{Rs_{SC}\cdot T}{C_{LA}(Rs_{SC}+Rs_{LA})};\right.\\
&-\frac{T}{C_{SC}}\left(1 - \frac{Rs_{SC}}{Rs_{SC}+Rs_{LA}}\right), -\frac{T}{C_{SC}}\left(1 - \frac{Rs_{SC}}{Rs_{SC}+Rs_{LA}}\right), -\frac{T}{C_{SC}}\left(1 - \frac{Rs_{SC}}{Rs_{SC}+Rs_{LA}}\right);\\
&-\frac{\eta_{LA}(k)\cdot Rs_{SC}\cdot T}{C_{N_{LA}}(k)(Rs_{SC}+Rs_{LA})}, -\frac{\eta_{LA}(k)\cdot Rs_{SC}\cdot T}{C_{N_{LA}}(k)(Rs_{SC}+Rs_{LA})}, -\frac{\eta_{LA}(k)\cdot Rs_{SC}\cdot T}{C_{N_{LA}}(k)(Rs_{SC}+Rs_{LA})};\\
&\left.\frac{T}{C_{LI}}, 0, 0; \frac{\eta_{LI}(k)\cdot T}{C_{N_{LI}}(k)}, 0, 0; 0, r_{H_2}(k)\cdot T, 0\right]\\
&C = \left[1 - \frac{Rs_{LA}}{Rs_{SC}+Rs_{LA}}, \frac{Rs_{LA}}{Rs_{SC}+Rs_{LA}},\ A_{LA}\left(1 - \frac{Rs_{LA}}{Rs_{SC}+Rs_{LA}}\right), 0, 0, 0; 0, 0, 1, 0, 0, 0; 0, 0, 0, 1, A_{LI}, 0;\right.\\
&\left.0, 0, 0, 0, 1, 0;\ 0, 0, 0, 0, 0, 1\right]\\
&D = \left[-\frac{Rs_{LA}\cdot Rs_{SC}}{Rs_{SC}+Rs_{LA}}, -\frac{Rs_{LA}\cdot Rs_{SC}}{Rs_{SC}+Rs_{LA}}, -\frac{Rs_{LA}\cdot Rs_{SC}}{Rs_{SC}+Rs_{LA}}; 0, 0, 0;\ Rs_{LI},\ 0,\ 0; 0, 0, 0; 0, 0, 0\right]\\
&E = \left[-\frac{Rs_{SC}\cdot T}{C_{LA}(Rs_{SC}+Rs_{LA})}; -\frac{T}{C_{SC}}\left(1 - \frac{Rs_{SC}}{Rs_{SC}+Rs_{LA}}\right); -\frac{\eta_{LA}(k)\cdot Rs_{SC}\cdot T}{C_{N_{LA}}(k)(Rs_{SC}+Rs_{LA})}; 0; 0; 0\right]\\
&F = \left[-\frac{T}{C_{LA}}\left(\frac{B_{LA}}{Rs_{SC}+Rs_{LA}} + C_{T_1}(k)\right); \frac{B_{LA}\cdot T}{C_{SC}(Rs_{SC}+Rs_{LA})}; -\frac{\eta_{LA}(k)\cdot B_{LA}\cdot T}{C_{N_{LA}}(k)(Rs_{SC}+Rs_{LA})}; -\frac{C_{T_2}(k)\cdot T}{C_{LI}}; 0; 0\right]\\
&G = \left[-\frac{Rs_{LA}\cdot Rs_{SC}}{Rs_{SC}+Rs_{LA}}; 0; 0; 0; 0\right]\\
&H = \left[B_{LA}\left(1 - \frac{Rs_{LA}}{Rs_{SC}+Rs_{LA}}\right); 0; B_{LI}; 0; 0\right]
\end{aligned}
\tag{43}
$$

Again, if simultaneous operation of the electrolyser and fuel cell is considered, the control vector would be redefined as $u(k) = \left[i_{LI}(k); i_{elec}(k); i_{fc}(k); i_{GRID}(k)\right]$ and the necessary modifications will be applied to (43) to update the model.

Finally, it is important to emphasise that the proposed LPV model can be adapted to fit the dynamics of the system under analysis. Based on the general expression (43), users can adjust the sampling period to capture slower variations, related to energy for example (longer sampling times), or faster variations, related to transient behaviours for example (shorter sampling times). This flexibility allows the model to be tailored for both long-term simulations and real-time control applications.

4. Results

To evaluate the performance of the developed model by means of the necessary tests, the microgrid depicted in Figure 1 has been sized. For this purpose, a typical consumption profile of a single-family house located in the climatic zone of the authors' Research Institute (Latitude: 37.2663800) was selected [71]. More details on this profile are provided below. The microgrid was sized according to the power and energy demanded (see Table 2) and is based on microgrid architectures previously used by the authors [71,72]. It should be noted that the optimal sizing of the microgrid is not the objective of this work, and alternative component values could have been chosen.

Table 2. Technical characteristics of the microgrid elements.

Component	Nominal Parameters
Solar PV mono-Si	10 kWp
LABB	30 × 12 V, 100 Ah (36 kWh)
LIBB	10 × 48 V, 100 Ah (48 kWh)
SCB	7 × 60 V, 20 F (1.3 kWh)
Alkaline electrolyser	1 Nm^3/h, 5 kWe
PEM fuel cell	3.4 kWp
Hydrogen tank	31.32 m^3 at 30 bar

The DC bus supporting the entire microgrid operates at a high voltage of 360 V, with renewable power supplied by a 10 kWp PV field. This voltage matches the typical operating input values of inverters required for power injection into the MEG, as well as powering electrolysers with power ratings in the kW range. Within its power range (see Table 2 for the nominal parameters of the microgrid elements), the microgrid can satisfy any consumption profile in both DC and AC.

The ESS of the microgrid is hybrid (HESS). For short-term response, a 36 kWh LABB and 1.3 kWh SCB array, both connected directly to the DC bus, are used. Additionally, a 48 kWh LIBB is available to operate as a medium-term ESS. Finally, the long-term ESS function is performed by an HBSS consisting of a 1 Nm^3/h alkaline electrolyser, a 31.32 m^3 at 30 bar hydrogen storage tank and a 3.4 kW PEM FC.

The microgrid includes a bidirectional connection to the MEG, enabling both energy purchase and sale. To integrate all components within the HVDC bus system, suitable power converters are used, as illustrated in Figure 1. Concerning the power converters depicted in Figure 4, these devices are omitted from the model. Although converters are essential for the operation and interconnection of the microgrid, from an energy management perspective, their main effect is conversion efficiency. Modern converters have average efficiencies of over 90%, which is why their efficiency has not been taken into account in the model. That said, if you want to incorporate the efficiency of any converter into the model, it is very simple: just enter the corresponding energy conversion efficiency in (43). For example, in the hydrogen system, only the generation and consumption rates of the electrolyzer and fuel cell, ($r_{H_2}(k)$, would need to be adjusted based on the efficiency of the converter.

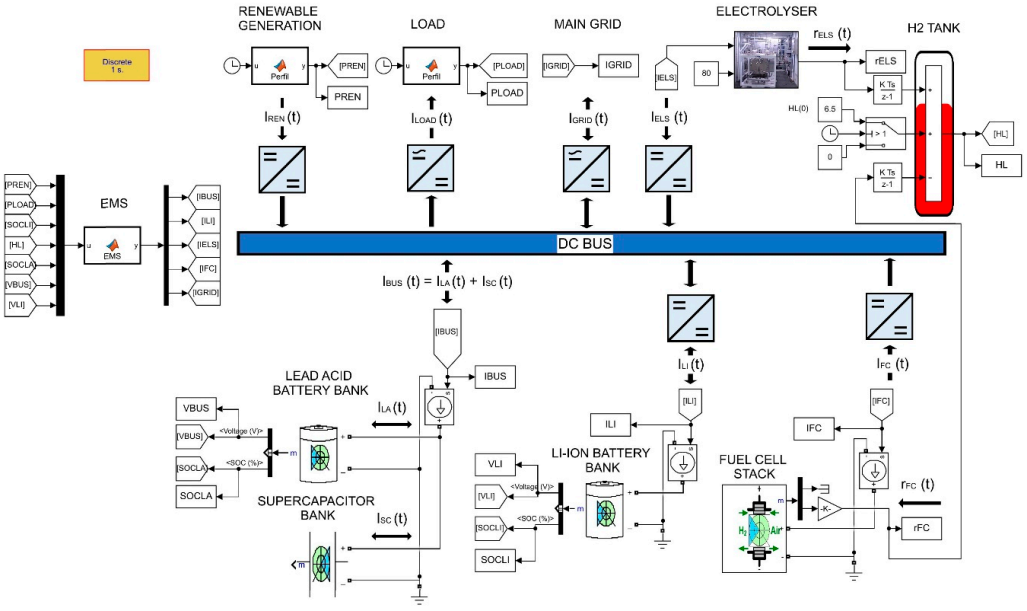

Figure 4. Reference microgrid model (RMM) implemented in MATLAB Simulink® R2019a.

Since the authors do not have access to a real microgrid with an architecture as complex as the one studied in this paper (Figure 1), the validation of the model's behaviour will be conducted by comparing it with validated, accurate and widely used reference models in the scientific literature. In this sense, the literature provides thoroughly tested and verified models (perhaps the best example being the models of MATLAB Simulink® R2019a) which serve as a perfect comparison to test the accuracy and usefulness of the developed microgrid model (hereinafter, DMM). With this goal in mind, a long-term simulation test of the DMM has been performed in MATLAB Simulink®. The simulations have been implemented on a Core™ i7-7700HQ (2.80 GHz) 16 GB RAM (Intel Corporation, Santa Clara, CA, USA) computer with Windows 10 Professional.

The individual models of each element, implemented in MATLAB Simulink® and already validated in the literature, were connected as shown in Figure 4 to implement the microgrid shown in Figure 1. This allowed the creation of the reference microgrid model (hereinafter RMM) in order to compare the performance of the DMM with it. To model the behaviour of the electrolyser (since MATLAB Simulink® does not include an electrolyser model among its libraries), the reference model based on the electrical equivalent double-layer model was used [73]. On the other hand, the PV generator, load consumption and the MEG were modelled solely based on their effect on the microgrid, i.e., as current sources/sinks.

The choice of the models already available in MATLAB Simulink® to build the RMM is justified by their widespread recognition, extensive use, and prior validation in the scientific literature with excellent results. However, it is very important to note that MATLAB Simulink® does not provide a microgrid model, such as the one developed in this work, which captures the dynamic of the entire microgrid depicted in Figure 1. Instead, it offers a collection of individual models (for each component) that, when properly interconnected, can configure a microgrid architecture such as the one in Figure 1 or another. Unfortunately, while the microgrid model presented in this work is fully reproducible, as all its analytical equations are available, the same cannot be said for some of the individual MATLAB Simulink® models used. These models, although they have shown very good performance in the scientific literature, have analytical expressions that are unknown, at least to the authors.

To validate the DMM, variable profiles of renewable generation and consumption were defined. Specifically, a PV generation profile based on the site's average annual generation was used. The selected consumption profile corresponds to that of a typical single-family home in the climate zone of the location of the microgrid.

To ensure the proper operation and validation of the DMM as a whole, it is necessary to design an EMS to determine the power setpoint of each element of the microgrid (in this case, the current setpoint). This EMS will be defined according to the established objectives and priorities, the generation and demand profile at each moment and the operating limits for each element of the microgrid.

Since the purpose of this work is not the development of an EMS but rather the validation of the DMM, a simplified EMS has been implemented for testing purposes and is described as follows. The main objective of the EMS is to guarantee the demand profile, regardless of the available renewable resource, while maximising the utilisation of the system's own resources (the HESS) and minimising reliance on the MEG. To this end, a hierarchy of priorities has been established in the roles of the various components comprising the HBSS.

The proposed priority-based EMS initially evaluates the sign of the current balance (i_{Bal}), as defined in (40), and the complete decision-making process is illustrated in Figure 5.

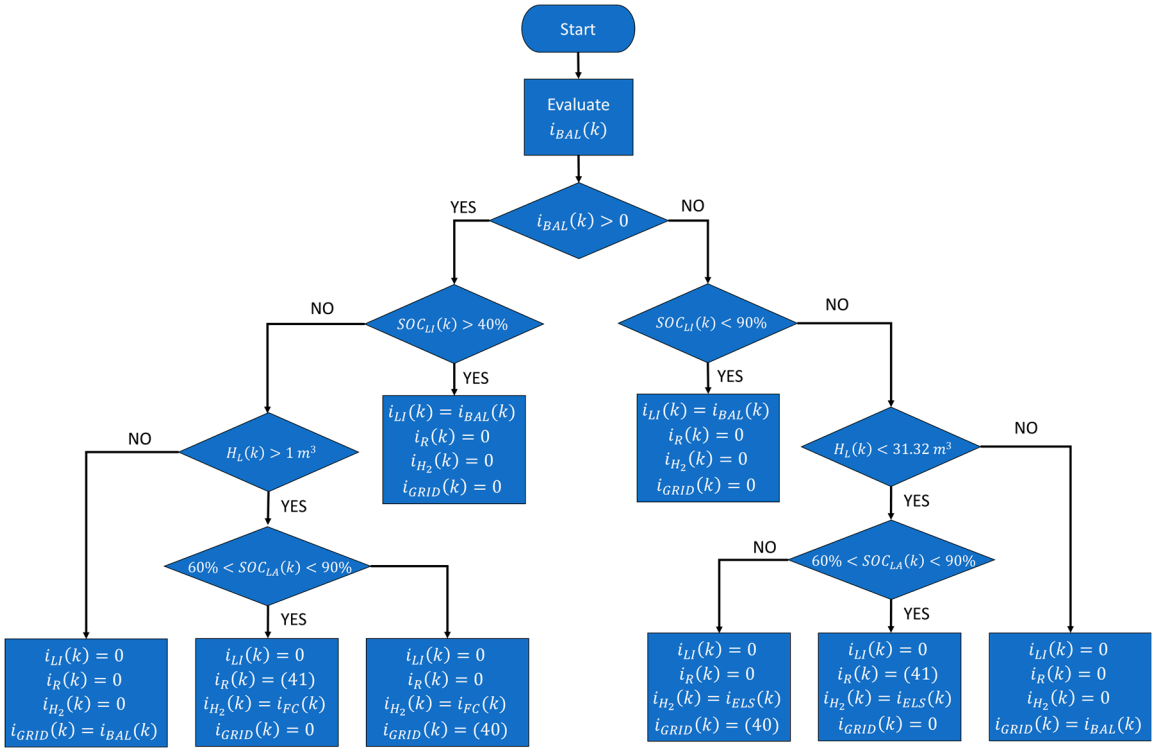

Figure 5. EMS decision-making process.

In the event of an energy surplus ($i_{Bal}(k) < 0$), the system prioritizes storing energy in the LIBB, which serves as the short-term ESS. Charging continues until the maximum state of charge is reached (SOC_{LI} = 90%). Once this threshold is attained, the EMS gives way to the HBSS, operating the electrolyzer at its rated power. To ensure compliance with (40) under all operating conditions, the LABB and the SCB operate according to (41), thereby sustaining electrolyzer operation provided the condition $SOC_{LA} \in$ [60%,90%] is satisfied. If the LABB reaches either of its capacity limits, the EMS activates the MEG to supply the electrolyzer. This mode of operation is maintained until the hydrogen storage tank reaches its maximum allowable capacity (H_L = 31.32 m^3 at 30 bar), after which all remaining surplus energy is exported directly to the MEG.

In the event of an energy deficit ($i_{Bal}(k) > 0$), the EMS applies a similar hierarchy of priorities, as depicted in Figure 5. The LIBB is initially discharged until its minimum state of charge is reached (SOC_{LI} = 40%). Subsequently, if hydrogen reserves are available, the fuel cell is activated to operate at a constant power level to supply the required energy. In parallel, the LABB and SCB operate according to (41), ensuring sustained fuel cell operation as long as the state of charge remains within the permitted range $SOC_{LA} \in$ [60%,90%]. If the LABB reaches one of its operating limits, the EMS triggers the MEG to provide additional support to the FC. This mode persists until the hydrogen storage level falls to its minimum allowable threshold (H_L = 1 m^3 at 30 bar), at which point the total energy deficit is compensated by importing electricity from the MEG.

The main parameters that configure the DMM and RMM are listed in Table 3. These parameters correspond to the elements in Figure 1. Table 3 also includes the initial test conditions chosen ($SOC_{LA}(0)$, $SOC_{LI}(0)$ and $H_L(0)$). In this case, the *SOCs* of the battery banks are at average values, while the *HL* is low, about 20% of its maximum capacity. Although other initial conditions could have been chosen, these have been deemed realistic.

Table 3. Model parameters.

Simulation							
Param.	**Value**	**Param.**	**Value**	**Param.**	**Value**	**Param.**	**Value**
T	1 s	$SOC_{LA}(0)$	80%	$SOC_{LI}(0)$	65%	$H_L(0)$	6.5 m^3
LABB model							
Param.	**Value**	**Param.**	**Value**	**Param.**	**Value**	**Param.**	**Value**
$V_{N_{LA}}$	360 V	$C_{N_{LA}}$	100 Ah	Rs_{LA}	0.75 Ω	C_{LA}	100 F
A_{LA}	30	B_{LA}	355	$Rp_{LA} = 1.91{\cdot}10^{-15}{\cdot}e^{(35{\cdot}SOC_{LA}(t))} + e^{(-2{\cdot}10^{-3}{\cdot}SOC_{LA}(t))}$			
LIBB model							
Param.	**Value**	**Param.**	**Value**	**Param.**	**Value**	**Param.**	**Value**
$V_{N_{LI}}$	480 V	$C_{N_{LI}}$	100 Ah	Rs_{LI}	0.75 Ω	C_{LI}	100 F
A_{LI}	30	B_{LI}	250	$Rp_{LI} = 1.91{\cdot}10^{-15}{\cdot}e^{(35{\cdot}SOC_{LI}(t))} + e^{(-2{\cdot}10^{-3}{\cdot}SOC_{LI}(t))}$			
SCB model							
Param.	**Value**	**Param.**	**Value**	**Param.**	**Value**	**Param.**	**Value**
$V_{N_{SC}}$	420 V	Rs_{SC}	25 mΩ	Rp_{SC}	5 kΩ	C_{SC}	20 F
ELS model							
Param.	**Value**	**Param.**	**Value**	**Param.**	**Value**	**Param.**	**Value**
R_{ELS}	2×10^{-4} Nm^3/Wh	N_{ELS}	30	$V_{N_{ELS}}$	62.5 V	$I_{N_{ELS}}$	80 A
T_{ELS}	80 °C						
FC model							
Param.	**Value**	**Param.**	**Value**	**Param.**	**Value**	**Param.**	**Value**
R_{FC}	6×10^{-4} Nm^3/Wh	N_{FC}	80	$V_{OC_{FC}}$	80.4 V	$V_{N_{FC}}$	54.6 V
$I_{N_{FC}}$	65 A	T_{FC}	65 °C				

Figure 6 illustrates the generation and consumption profile of the microgrid over a 24-h period, following the adopted sign criteria. $P_{LA} + P_{SC}$ means that the LABB and SCB operate together in parallel. On the scale of the simulation graphs, the individual operation of the SCB is not discernible due to its much faster response compared to the LABB (note that the fundamental task of the SCB is to mitigate instantaneous peaks on the DC bus [18]).

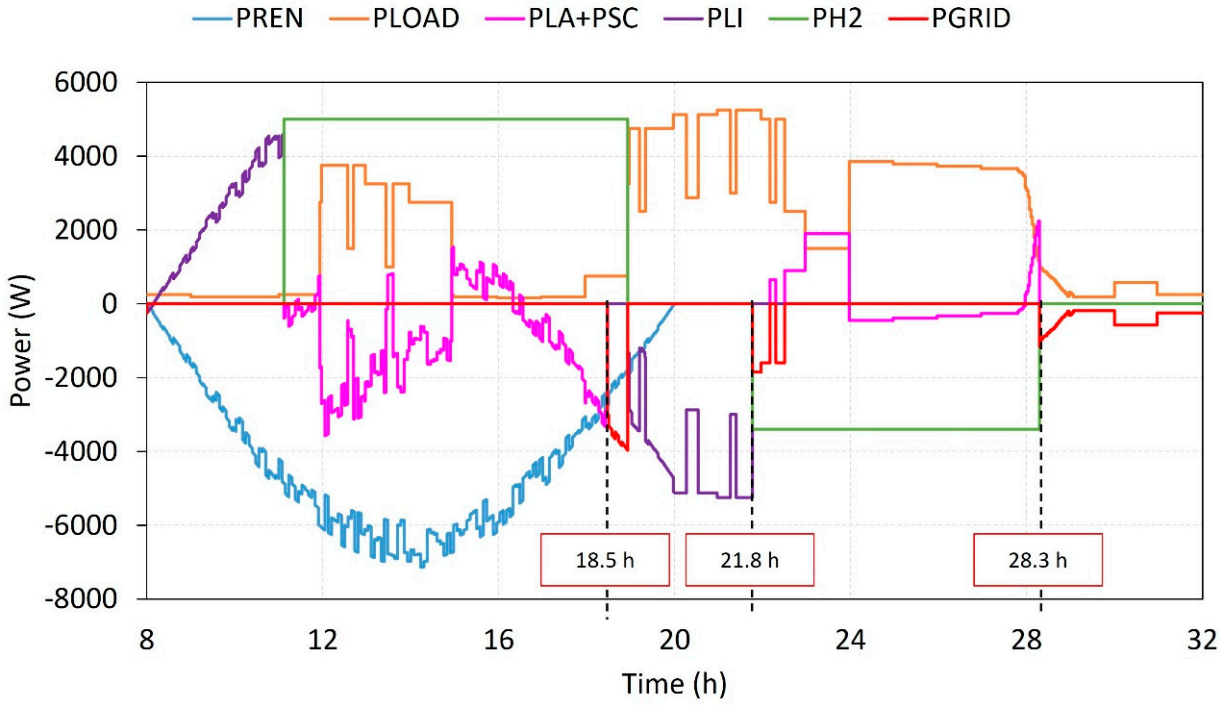

Figure 6. Microgrid power variables: renewable source (PREN), loads (PLOAD), LABB and SCB set (PLA+PSC), hydrogen-based storage system (PH2) and MEG (PGRID).

Figures 7–9 show the behaviour of LIBB, LABB and H_L, respectively. Note the comparison between DMM and RMM.

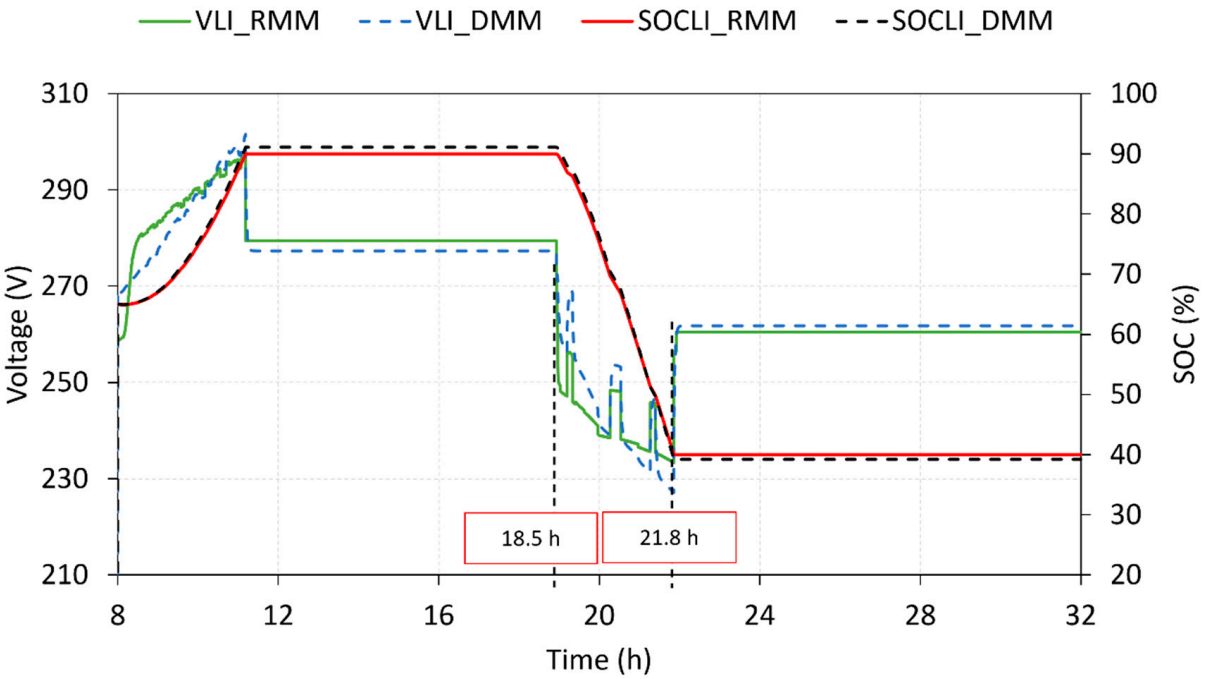

Figure 7. LIBB voltage and SOC for the reference (RMM) and developed (DMM) models.

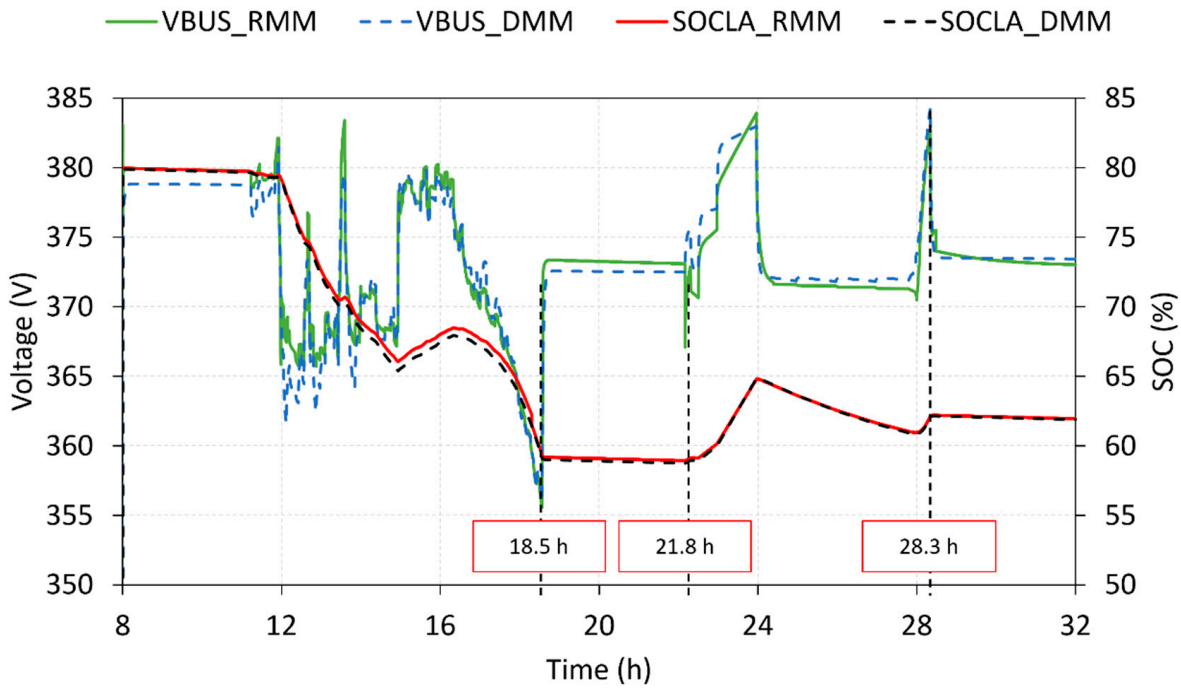

Figure 8. DC bus voltage and SOC of the LABB for the reference (RMM) and developed (DMM) models.

Finally, Figure 10 compares the operating currents of the LABB (i_{LA}) and SCB ($i_{Rs_{SC}}$) for both the RMM and the DMM. For the RMM, the currents were measured directly, whereas for the DMM, they were calculated analytically using expressions (44) and (45), which are derived from the current balance and state-space model in Equations (41) and (43), respectively, and from the equivalent circuit in Figure 2.

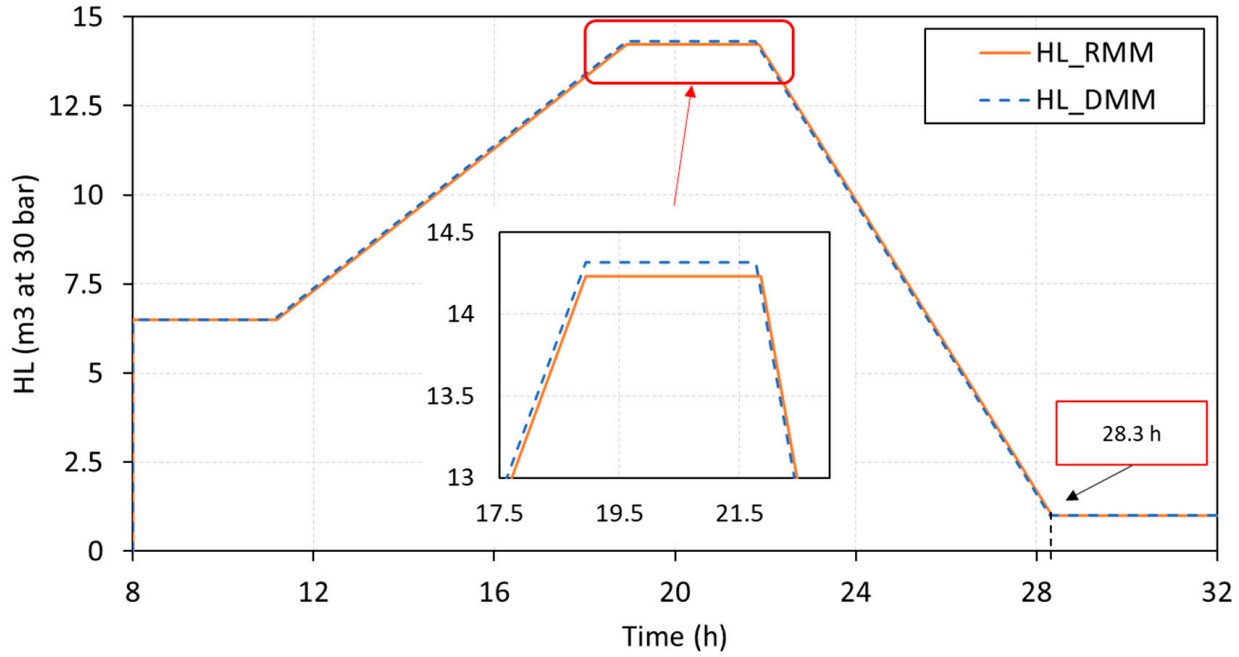

Figure 9. Hydrogen level in the pressure tank for the reference (RMM) and developed (DMM) models.

$$i_{Rs_{SC}}(k) = \frac{v_{BUS}(k) - v_{C_{SC}}(k)}{Rs_{SC}} \tag{44}$$

$$i_{LA}(k) = i_R(k) - i_{Rs_{SC}}(k) \tag{45}$$

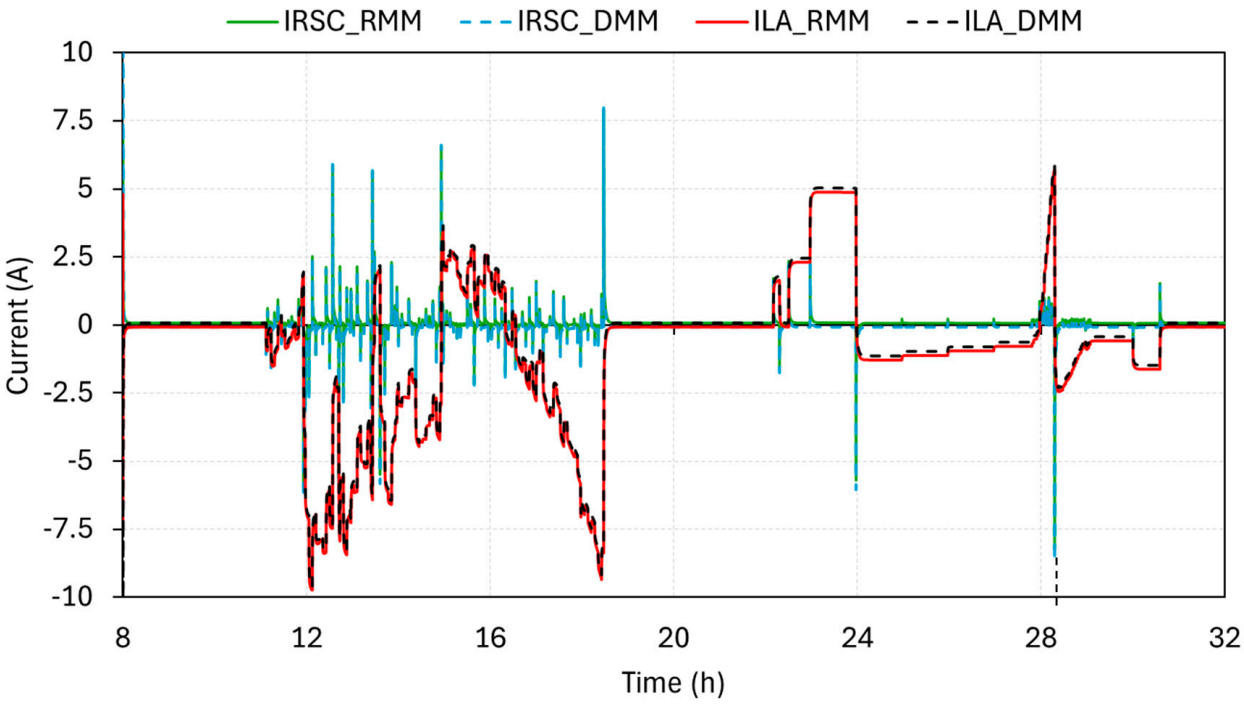

Figure 10. Operating current of the LABB (ILA) and SCB (IRSC) for the reference (RMM) and developed (DMM) models.

5. Discussion

To understand the operation of the microgrid, it is essential to understand the operation of Equation (40), which ensures Kirchhoff's law holds true on the DC bus at all times. The renewable power available is not controlled by the EMS, so the corresponding

consumptions must be generated (this is controlled by the EMS) for Equation (40) to be satisfied. The consumptions that can be activated by the EMS is LIBB charging, hydrogen production, and the energy sales to the MEG. However, the EMS cannot control LABB and SCB, nor the consumption of internal microgrid loads.

According to the generation and demand profile, Figure 6, the microgrid starts the morning hours in an energy surplus situation, which is maintained over time during the period 8 h $\leq t \leq$ 19 h. At 8 am local time (Central European Time (CET), UTC +1 from November to March and UTC +2 the rest of the year), the sun is already strong enough to start generating power on the photovoltaic panels. Based on the operation of the proposed EMS and the role of the ESS, first, all the surplus energy is used to recharge the LIBB, leading to a consequent increase in its voltage and SOC values (V_{LI} and SOC_{LI}, respectively), until the preset maximum value of SOC_{LI} = 90% is reached at $t \approx$ 11 h (approximate charging time of 3 h, see Figure 7).

Returning to Figure 6, since there is very little load demand on the microgrid during the LIBB charging period, the profiles of P_{REN} and P_{LI} are practically opposite. Consequently, the resulting power input/output to the DC bus and, therefore, to the LABB and SCB set ($P_{LA} + P_{SC}$) is nearly zero. As a result, SOC_{LA} and the DC bus voltage (V_{BUS}) remain stable during this time interval: $V_{BUS} \approx$ 380 V and $SOC_{LA} = SOC_{LA}(0)$ = 80% (Figure 8). About t = 11 h (Figure 6), the EMS disconnects the LIBB from the DC bus via its power converter (Figure 1) to avoid overcharging. Therefore, from this point onward, SOC_{LI} and V_{LI} remain constant over time, Figure 7.

Surplus renewable energy on the DC bus is used by the EMS to produce renewable hydrogen by running the electrolyser at rated power, Figure 6. The EMS performs this operation because the hydrogen level in the pressure tank is well below the maximum (31.32 m^3), Figure 9. As time progresses and renewable energy decreases, the power balance is supported by the LABB (Figure 6). This causes successive charging and discharging processes of the LABB according to the bus power balance at each moment (see Figure 6, period 11 h $\leq t \leq$ 18.5 h). During this period, three charging processes were observed with a total duration of approximately 1.62 h, and up to four discharging processes with a total duration of 5.86 h (see Figure 6). It should be noted that to avoid an energy deficit in the bus, the LABB must supply the necessary energy. This, logically, causes that the SOC of the LABB to decrease until it reaches its established minimum value (60%, 18.5 h, Figure 8). Actually, the SOC decreases a bit more due to uncontrolled download speed on the bus (EMS should act a bit earlier). At this point, if the EMS were to lead to $P_{LA} + P_{SC} = 0$, there would be surplus power on the DC bus because renewable power is still available (Figure 6). For this reason, the EMS keeps the electrolyser running (since there is still capacity available in the hydrogen tank, Figure 9), although to balance the bus it injects the necessary power (that which allows (40) to be satisfied) from the MEG. This causes $P_{LA} + P_{SC}$ to drop to zero (Figure 6), and SOC_{LA} and V_{BUS} remain constant (Figure 8). The question arises as to why, at 18.5 h, the EMS injects from the MEG and not from the LIBB, which is charged. It is simply a matter of how the EMS is programmed, which, of course, can be changed, although the design and optimization of the EMS is not the subject of this article.

Around 18.9 h, due to the consumption of the internal loads of the microgrid, P_{LOAD} increases considerably, and the demand profile exceeds renewable generation, which gradually diminishes as the day progresses, Figure 6. Then, to balance the DC bus, the EMS turns off the electrolyser and connects the LIBB. This leads to an associated discharge process lasting 2.9 h, causing its voltage and SOC to decrease until reaching the preset minimum level, SOC_{LI} = 40% at t = 21.8 h, Figure 7. Note that, unlike LABB, EMS can now precisely control the SOC of LIBB, as it disconnects it from the bus via its power converter

to avoid over-discharge. Therefore, SOC_{LI} and V_{LI} remain constant over time, Figure 7. Since until 21.8 h the power balance is guaranteed exclusively by the LIBB, the SOC_{LA} is kept constant and the bus voltage, Figure 8. This means that $P_{LA} + P_{SC} = 0$ during this interval, Figure 6.

From 21.8 h onwards, because there is an energy deficit in the microgrid (Figure 6) and there is enough hydrogen stored in the tank (Figure 9), the EMS turns on FC at rated power. However, this is not enough to balance the bus, so the EMS supplies the necessary power (the one that allows to satisfy (40)) from the MEG. Note that, during intervals when the FC can maintain balance on the bus by itself, P_{GRID} is reduced to zero and the LABB + SCB set is charged from the bus to meet (40).

The FC operation continues until H_L reaches the minimum established value (1 m^3) at 28.3 h, Figures 6 and 8. From 21.8 h to 28.3 h, oscillations in SOC_{LA} occur, particularly when the MEG is disconnected. This is because $SOC_{LA} > 60\%$ and can balance the bus by itself, Figures 6 and 8. These variations in the operation of the LABB+SCB set result in charging and discharging processes during the indicated interval, having a duration of 1.73 h and 4.2 h, respectively, according to the power balance.

Finally, after 28.3 h, the MEG guarantees balance on the bus by supplying the small amount of power required by the microgrid.

As already mentioned, the direct parallel connection of the LABB and SCB to the DC bus is fundamental to the microgrid's stability, creating a synergistic partnership that optimises performance. As shown in Figure 8, the bus voltage fluctuations are maintained within an acceptable range of 355 V $\leq$ V_BUS $\leq$ 385 V (an 8.3% swing), demonstrating the damping effect resulting from this configuration.

The operational dynamics of this hybrid storage system are clearly illustrated in Figure 10, which shows the respective currents, according to Figure 2, of the LABB (i_{LA}) and the SCB ($i_{Rs_{SC}}$). The SCB demonstrates its fundamental role by responding quickly and absorbing instantaneous current transients, while the LABB balances the power to maintain steady-state equilibrium and, consequently, the voltage on the DC bus. This effective distribution of roles is the direct cause of the dampening effect observed. This relatively smooth dynamics on the DC bus is crucial for improving the overall performance of the microgrid and the lifespan of its components. As an immediate effect, the SCB directly contributes to extending the service life of the LABB, as it protects it from instantaneous current spikes that are very harmful to it. Furthermore, the stabilized bus voltage improves general microgrid reliability by preventing sudden voltage drops and avoiding safety-driven disconnections of other sensitive components, thereby ensuring more stable and continuous operation.

After analysing the behaviour of the microgrid over time, the results demonstrate the exceptional performance of the proposed LPV model through detailed comparisons between the DMM and RMM. As shown in Figures 7–9, the model achieves nearly perfect alignment with the actual system behaviour across all critical variables: the LIBB voltage and SOC (Figure 7), DC bus voltage and LABB SOC (Figure 8), and stored hydrogen levels (Figure 9). This remarkable accuracy is maintained despite the strong nonlinearities of the microgrid, evident in the RMM (Figure 4). Table 4 quantitatively confirms that the average errors, MAE, RAE and RMSE values remain below 1.2% for all output variables, where it is crucial to note that these metrics only reflect the differences between the models and not the absolute accuracy. Therefore, in view of the results, it can only be inferred that DMM and RMM are very close, but not that one is better than the other in terms of accuracy.

Table 4. Error analysis.

Param.	Average Error	RAE	MAE	RMSE
v_{BUS}	0.194 V (0.051%)	0.259 V (0.07%)	0.883 V (0.236%)	1.969 V (0.527%)
SOC_{LA}	0.206%	0.035%	0.208%	0.363%
v_{LI}	0.005 V (−0.002%)	0.217 V (0.081%)	2.330 V (0.871%)	3.195 V (1.195%)
SOC_{LI}	−0.149%	0.037%	0.830%	0.889%
H_L	−0.012 m^3 (−0.152%)	0.016 m^3 (0.199%)	0.062 m^3 (0.757%)	0.075 m^3 (0.915%)
i_{LA}	−0.02 A (1.05%)	0.012 A (−1.07%)	0.02 A (−1.06%)	0.057 A (−1.16%)
$i_{Rs_{SC}}$	0.001 A (−0.09%)	0.003 A (−0.49%)	0.001 A (−0.9%)	0.009 A (−1.2%)

Based on the results and the discussion of these, the proposed LPV model offers significant advantages over traditional modelling approaches. Compared to LTI models, it successfully captures the nonlinear dynamics of the microgrid while maintaining computational efficiency, as demonstrated by the near-perfect alignment of the DMM behaviour with that of the highly nonlinear RMM (Figures 7–9). Compared to complex nonlinear models, the LPV approach demonstrates superior practicality by overcoming two critical limitations: computational costs (achieving a 24-h simulation in just 1.49 s compared to 2.96 s for RMM) and the ability to provide unified behaviour and representation of the microgrid, rather than focusing on individual components. This balance is achieved thanks to the linear structure of the model, its compact formulation (43), and the efficient parameter update mechanism, which captures the power and energy flows of the entire microgrid in each sampling.

These results conclusively demonstrate that the proposed model effectively captures the behaviour of a complex and non-linear system, such as the microgrid architecture presented in Figure 1, while preserving simplicity and computational efficiency. This approach offers a comprehensive framework for the thorough analysis of this type of microgrid and others.

Finally, since P_{REN} and P_{LOAD} are treated as independent input variables, the model is independent of the specific type of renewable generators (e.g., solar, wind, or hybrid systems) and load consumption patterns in the microgrid. This unique combination of accuracy and efficiency makes the proposed framework widely applicable to various microgrid configurations without the need for structural modifications, making it especially valuable for real-time control applications and large-scale microgrid studies, while circumventing shortcomings of current modelling methodologies.

6. Conclusions

This document presents a comprehensive state-space model specifically developed for model-based controller design, system sizing optimization and in-depth analysis of renewable microgrids incorporating complex HESS.

The microgrid under investigation, which holds significant scientific interest, incorporates a HESS comprising a HBSS, a BSS and a SCB. These components are interconnected through a HV-DC bus, enabling a flexible and robust power distribution architecture. The DC bus is stabilized by a direct passive parallel configuration of the BSS and SCB, ensuring voltage stability and reliable system performance.

The proposed model employs a full-state representation that captures the dynamic interactions among all microgrid components. The state matrix, although linear at each sampling interval, evolves over time, embodying an LPV structure that mirrors the system's nonlinear behaviour. Compared to conventional methods, whether static, simplified LTI models or computationally intensive nonlinear models, the proposed LPV-based approach stands out by offering a structured control-oriented modelling framework that is both accurate and computationally efficient. Its ability to represent the non-ideal and time-

varying behaviour of a system through linear analysis is especially beneficial for the design of high-performance, real-time EMS controllers, such as MPCs. This integration of a comprehensive and exhaustive microgrid model adapted to control applications represents a significant advance over existing approaches.

Simulation results demonstrate the model's effectiveness in reproducing real microgrid behaviour while maintaining low computational requirements. Its balance between accuracy and efficiency makes it especially suited for real-time EMS applications.

Looking ahead, work will focus on the experimental validation of this model within an operational microgrid. Building on the model developed, the next phase of the research will consist of implementing and testing an advanced EMS based on MPC, with the aim of refining and optimizing energy management strategies for microgrids in real-world conditions. This practical deployment will offer empirical validation of the model's effectiveness, reinforcing its applicability in real-world scenarios. By narrowing the gap between theoretical development and practical implementation, it represents a significant advancement in the field. Moreover, this contribution is expected to actively support the broader adoption of renewable microgrids, providing a timely and robust solution to pressing energy and geopolitical challenges.

Author Contributions: Conceptualization, J.M.A.M.; Methodology, F.J.V.F. and F.S.M.; Software, F.J.V.F.; Formal analysis, J.M.A.M. and F.S.M.; Investigation, F.J.V.F. and F.S.M.; Writing—original draft, F.J.V.F.; Writing—review & editing, J.M.A.M. and F.S.M.; Funding acquisition, J.M.A.M. All authors have read and agreed to the published version of the manuscript.

Funding: This work is a contribution of Project PID2023-148456OB-C41 supported by the Spanish Ministry of Economy and Competitiveness.

Data Availability Statement: The original contributions presented in this study are included in the article. Further inquiries can be directed to the corresponding author.

Conflicts of Interest: The authors declare no conflict of interest.

Abbreviations

Acronyms

BB	Battery bank
BSS	Battery-based storage system
DMM	Developed microgrid model
EMS	Energy management system
ESS	Energy storage system
FC	Fuel cell
H2V	Home-to-vehicle
HBSS	Hydrogen-based storage system
HESS	Hybrid energy storage system
HL	Hydrogen level
HVDC	High voltage DC
KCL	Kirchhoff's Current Law
KVL	Kirchhoff's Voltage Law
LABB	Lead-acid battery bank
LIBB	Lithium-ion battery bank
LPV	Linear parameter-varying
LTI	Linear time invariant
MEG	Main electricity grid
MPC	Model-based predictive control
MPPT	Maximum power point tracker
PEM	Polymer electrolyte membrane

PV	Photovoltaic
PWL	Piecewise-linear
RMM	Reference microgrid model
RMSE	Root mean square error
SCB	Supercapacitor bank
SOC	State of charge
V2H	Vehicle-to-home
Symbols	
C_x	Parallel internal capacitance of LABB ($x = LA$), LIBB ($x = LI$) or SCB ($x = SC$) (F)
$C_{N_x}(t)$	Nominal capacity of LABB ($x = LA$) or LIBB ($x = LI$) (Ah)
F	Faraday constant (26.81 Ah/eq)
$H_L(t)$	Level of hydrogen stored in the hydrogen tank (Nm^3 or m^3 at 30 bar)
$i_{BAL}(t)$	Current balance in the DC bus (A)
$i_x(t)$	Charge/Discharge current of LABB ($x = LA$), LIBB ($x = LI$) or SCB ($x = SC$), or operating current of renewable generation ($x = REN$), load consumption ($x = LOAD$), electrolyser ($x = ELS$), fuel cell ($x = FC$), HBSS ($x = H_2$), or MEG ($x = GRID$) (A)
i_{N_x}	Nominal current of ELS ($x = ELS$) or FC ($x = FC$) (A)
$i_R(t)$	Charge/Discharge current of the set of LABB and SCB (A)
$i_{Rp_x}(t)$	Current flowing through the parallel resistor of LABB ($x = LA$), LIBB ($x = LI$) or SCB ($x = SC$) (A)
$i_{Rs_{SC}}(t)$	Current flowing through the SCB series resistor (A)
M_{H_2}	Molecular hydrogen molar mass (2.02 g/mol)
N_x	Number of cells of the electrolyser ($x = ELS$) or fuel cell stack ($x = FC$).
$\eta_x(t)$	Charging/discharging performance of LABB ($x = LA$) or LIBB ($x = LI$)
$P_x(t)$	Charge/Discharge power of LABB ($x = LA$), LIBB ($x = LI$) or SCB ($x = SC$), or operating power of renewable generation ($x = REN$), load consumption ($x = LOAD$), electrolyser ($x = ELS$), fuel cell ($x = FC$), HBSS ($x = H_2$), or MEG ($x = GRID$) (A)
r_x	Electrolyser hydrogen production ratio ($x = ELS$) or FC hydrogen consumption ratio ($x = FC$) (Nm^3/A)
$r_{H_2}(t)$	Hydrogen consumption/production ratio of the HBSS (Nm^3/A)
ρ_{H_2}	Molecular hydrogen gas density (0.0899 kg/Nm^3)
Rp_x	Parallel internal resistance of LABB ($x = LA$), LIBB ($x = LI$) or SCB ($x = SC$) (Ω)
Rs_x	Series internal resistance of LABB ($x = LA$), LIBB ($x = LI$) or SCB ($x = SC$) (Ω)
$SOC_x\ (t)$	State of charge of LABB ($x = LA$) or LIBB ($x = LI$)
$v_{BUS}(t)$	DC Bus voltage (V)
$v_x(t)$	Voltage at LABB ($x = LA$), LIBB ($x = LI$) or SCB ($x = SC$) capacitance (V)
V_{N_x}	Nominal voltage of LABB ($x = LA$), LIBB ($x = LI$), SCB ($x = SC$), ELS ($x = ELS$) or FC ($x = FC$) (V)
$v_{OC_x}(t)$	Open circuit voltage of LABB ($x = LA$), LIBB ($x = LI$) or FC ($x = FC$) (V)
T	Sample time (s)
T_x	Operating temperature of ELS ($x = ELS$) or FC ($x = FC$) (A) (°C)
z	Number of electrons involved in the reduction − oxidation reaction ($z = 2$)

References

1. Barra, C.; Falcone, P.M.; Giganti, P. Exploring the impact of economic, climate, and energy policy uncertainty on the Environmental Kuznets Curve: International evidence. *Int. Econ.* **2025**, *182*, 100592. [CrossRef]
2. Giganti, P.; Barra, C.; Falcone, P.M. Unveiling the nexus of institutional quality and renewable energy utilizing a Topic Modelling approach. *Renew. Sustain. Energy Rev.* **2025**, *214*, 115516. [CrossRef]
3. Vivas, F.J.; De las Heras, A.; Segura, F.; Andújar, J.M. A review of energy management strategies for renewable hybrid energy systems with hydrogen backup. *Renew. Sustain. Energy Rev.* **2018**, *82*, 126–155. [CrossRef]
4. Zidane, T.E.K.; Muis, Z.A.; Ho, W.S.; Zahraoui, Y.; Aziz, A.S.; Su, C.L.; Mekhilef, S.; Elia Campana, P. Power systems and microgrids resilience enhancement strategies: A review. *Renew. Sustain. Energy Rev.* **2025**, *207*, 114953. [CrossRef]
5. Uddin, M.; Mo, H.; Dong, D.; Elsawah, S.; Zhu, J.; Guerrero, J.M. Microgrids: A review, outstanding issues and future trends. *Energy Strateg. Rev.* **2023**, *49*, 101127. [CrossRef]

6. Punitha, S.; Subramaniam, N.P.; Raj, P.A.D.V. A comprehensive review of microgrid challenges in architectures, mitigation approaches, and future directions. *J. Electr. Syst. Inf. Technol.* **2024**, *11*, 60. [CrossRef]
7. Kazerani, M.; Tehrani, K. Grid of Hybrid AC/DC Microgrids: A New Paradigm for Smart City of Tomorrow. In Proceedings of the 2020 IEEE 15th International Conference of System of Systems Engineering (SoSE), Budapest, Hungary, 2–4 June 2020; pp. 175–180. [CrossRef]
8. Hajiaghasi, S.; Salemnia, A.; Hamzeh, M. Hybrid energy storage system for microgrids applications: A review. *J. Energy Storage* **2019**, *21*, 543–570. [CrossRef]
9. He, W.; King, M.; Luo, X.; Dooner, M.; Li, D.; Wang, J. Technologies and economics of electric energy storages in power systems: Review and perspective. *Adv. Appl. Energy* **2021**, *4*, 100060. [CrossRef]
10. Monforti Ferrario, A.; Bartolini, A.; Segura Manzano, F.; Vivas, F.J.; Comodi, G.; McPhail, S.J.; Andujar, J.M. A model-based parametric and optimal sizing of a battery/hydrogen storage of a real hybrid microgrid supplying a residential load: Towards island operation. *Adv. Appl. Energy* **2021**, *3*, 100048. [CrossRef]
11. Van, L.P.; Do Chi, K.; Duc, T.N. Review of hydrogen technologies based microgrid: Energy management systems, challenges and future recommendations. *Int. J. Hydrogen Energy* **2023**, *48*, 14127–14148. [CrossRef]
12. Jain, D.; Saxena, D. Comprehensive review on control schemes and stability investigation of hybrid AC-DC microgrid. *Electr. Power Syst. Res.* **2023**, *218*, 109182. [CrossRef]
13. Alam, M.S.; Al-Ismail, F.S.; Rahman, S.M.; Shafiullah, M.; Hossain, M.A. Planning and protection of DC microgrid: A critical review on recent developments. *Eng. Sci. Technol. Int. J.* **2023**, *41*, 101404. [CrossRef]
14. Vivas, F.J.; Segura, F.; Andújar, J.M.; Calderón, A.J.; Isorna, F. Battery-based storage systems in high voltage-DC bus microgrids. A real-time charging algorithm to improve the microgrid performance. *J. Energy Storage* **2022**, *48*, 103935. [CrossRef]
15. Zhang, L.; Hu, X.; Wang, Z.; Ruan, J.; Ma, C.; Song, Z.; Dorrell, D.G.; Pecht, M.G. Hybrid electrochemical energy storage systems: An overview for smart grid and electrified vehicle applications. *Renew. Sustain. Energy Rev.* **2021**, *139*, 110581. [CrossRef]
16. Ferahtia, S.; Houari, A.; Cioara, T.; Bouznit, M.; Rezk, H.; Djerioui, A. Recent advances on energy management and control of direct current microgrid for smart cities and industry: A Survey. *Appl. Energy* **2024**, *368*, 123501. [CrossRef]
17. Vivas, F.J.; Segura, F.; Andújar, J.M. Fuzzy logic-based energy management system for grid-connected residential DC microgrids with multi-stack fuel cell systems: A multi-objective approach. *Sustain. Energy Grids Netw.* **2022**, *32*, 100909. [CrossRef]
18. Caparrós Mancera, J.J.; Saenz, J.L.; López, E.; Andújar, J.M.; Segura Manzano, F.; Vivas, F.J.; Isorna, F. Experimental analysis of the effects of supercapacitor banks in a renewable DC microgrid. *Appl. Energy* **2022**, *308*, 118355. [CrossRef]
19. Naderi, E.; Bibek, K.C.; Ansari, M.; Asrari, A. Experimental Validation of a Hybrid Storage Framework to Cope with Fluctuating Power of Hybrid Renewable Energy-Based Systems. *IEEE Trans. Energy Convers.* **2021**, *36*, 1991–2001. [CrossRef]
20. Sohaib, M.; Akram, A.S.; Choi, W. Analysis of Aging and Degradation in Lithium Batteries Using Distribution of Relaxation Time. *Batteries* **2025**, *11*, 34. [CrossRef]
21. Altaf, M.T.; Fatima, H.; Jamil, M. Effect of peak current on battery performance. In Proceedings of the Conference on Recent Advances in Electrical, Electronics & Digital Healthcare Technologies (REEDCON), New Delhi, India, 1–3 May 2023; pp. 611–614. [CrossRef]
22. Ravada, B.R.; Tummuru, N.R.; Ande, B.N.L. Photovoltaic-Wind and Hybrid Energy Storage Integrated Multisource Converter Configuration-Based Grid-Interactive Microgrid. *IEEE Trans. Ind. Electron.* **2021**, *68*, 4004–4013. [CrossRef]
23. Jing, W.; Lai, C.H.; Wong, W.S.H.; Wong, M.L.D. Dynamic power allocation of battery-supercapacitor hybrid energy storage for standalone PV microgrid applications. *Sustain. Energy Technol. Assess.* **2017**, *22*, 55–64. [CrossRef]
24. Pajares, A.; Vivas, F.J.; Blasco, X.; Herrero, J.M.; Segura, F.; Andújar, J.M. Methodology for energy management strategies design based on predictive control techniques for smart grids. *Appl. Energy* **2023**, *351*, 121809. [CrossRef]
25. Polimeni, S.; Meraldi, L.; Moretti, L.; Leva, S.; Manzolini, G. Development and experimental validation of hierarchical energy management system based on stochastic model predictive control for Off-grid Microgrids. *Adv. Appl. Energy* **2021**, *2*, 100028. [CrossRef]
26. Andújar, J.M.; Vivas, F.J.; Segura, F.; Calderón, A.J. Integration of air-cooled multi-stack polymer electrolyte fuel cell systems into renewable microgrids. *Int. J. Electr. Power Energy Syst.* **2022**, *142*, 108305. [CrossRef]
27. Rodriguez, M.; Arcos-Aviles, D.; Guinjoan, F. Simple fuzzy logic-based energy management for power exchange in isolated multi-microgrid systems: A case study in a remote community in the Amazon region of Ecuador. *Appl. Energy* **2024**, *357*, 122522. [CrossRef]
28. Oussama, H.; Amine, H.M.; Mohamed Amine, S.; Aissa, B.; Abdeselem, C.; Othmane, A. Intelligent Energy Management Strategy For Multi-Sources Isolated DC-Microgrid. In Proceedings of the 2023 Second International Conference on Energy Transition and Security (ICETS), Adrar, Algeria, 12–14 December 2023; pp. 1–5. [CrossRef]
29. Fathy, A.; Alfayyadh, S.A. Efficient energy management strategy for reducing the hydrogen consumption of hybrid fuel cell/supercapacitor/battery microgrid. *Int. J. Hydrogen Energy* **2025**, *162*, 150715. [CrossRef]

30. Shuvo, J.I.; Badoruzzaman, M.; Anik, S.T.I.; Ahmad, S.; Ahmed, T.; Karimi, M. Hybrid energy storage power management system harnessing battery-supercapacitor synergy for grid-isolated DC microgrid. *J. Energy Storage* **2025**, *119*, 116170. [CrossRef]
31. Papageorgiou, P.; Oureilidis, K.; Tsakiri, A.; Christoforidis, G. A Modified Decentralized Droop Control Method to Eliminate Battery Short-Term Operation in a Hybrid Supercapacitor/Battery Energy Storage System. *Energies* **2023**, *16*, 2858. [CrossRef]
32. Rezk, H.; Fathy, A. Hydrogen reduction-based energy management strategy of hybrid fuel cell/PV/battery/supercapacitor renewable energy system. *J. Energy Storage* **2024**, *86*, 111316. [CrossRef]
33. Alharbi, A.G.; Olabi, A.G.; Rezk, H.; Fathy, A.; Abdelkareem, M.A. Optimized energy management and control strategy of photovoltaic/PEM fuel cell/batteries/supercapacitors DC microgrid system. *Energy* **2024**, *290*, 130121. [CrossRef]
34. Yu, Z.; Long, J. Review on Advanced Model Predictive Control Technologies for High-Power Converters and Industrial Drives. *Electronics* **2024**, *13*, 4969. [CrossRef]
35. Vidyasagar, P.; Shanti Swarup, K. LTI-MPC for the Micro-grid Control. In *Design and Development of Model Predictive Primary Control of Micro Grids*; Springer Tracts in Electrical and Electronics Engineering; Springer: Singapore, 2023.
36. Villalón, A.; Rivera, M.; Salgueiro, Y.; Muñoz, J.; Dragičević, T.; Blaabjerg, F. Predictive control for microgrid applications: A review study. *Energies* **2020**, *13*, 2454. [CrossRef]
37. Zhang, Y.; Xue, Q.; Gao, D.; Shi, W.; Yu, W. Two-level model predictive control energy management strategy for hybrid power ships with hybrid energy storage system. *J. Energy Storage* **2022**, *52*, 104763. [CrossRef]
38. Tabrizi, S.Y.; Mahdavi, M.S.; Khorsandi, A.; Gharehpetian, G.B. Model Predictive Control of Hybrid Energy Storage System of Amirkabir DC Microgrid. In Proceedings of the 2023 13th Smart Grid Conference (SGC), Tehran, Iran, 5–6 December 2023; pp. 1–6. [CrossRef]
39. Wang, L. Oilfield Microgrid-Oriented Supercapacitor-Battery Hybrid Energy Storage System with Series-Parallel Compensation Topology. *Processes* **2025**, *13*, 1689. [CrossRef]
40. Punna, S.; Banka, S.; Salkuti, S.R. Optimal Energy Management Scheme of Battery Supercapacitor-Based Bidirectional Converter for DC Microgrid Applications. *Information* **2022**, *13*, 350. [CrossRef]
41. Ma, T.; Yang, H.; Lu, L. Development of hybrid battery-supercapacitor energy storage for remote area renewable energy systems. *Appl. Energy* **2015**, *153*, 56–62. [CrossRef]
42. Seedahmed, M.M.A.; Ramli, M.A.M.; Abusorrah, A.; Alqahtani, M.M. Control-Oriented Model of an Optimally Designed Hybrid Storage System for a Standalone Microgrid. *IEEE Access* **2023**, *11*, 119161–119186. [CrossRef]
43. Errakkas, K.; Kissaoui, M.; Lajouad, R.; El Magri, A.; Atifi, Y.; Khayat, A. A Model Predictive Control Strategy for improvement Performance in PV-Battery-Hydrogen DC Islanded Microgrid. *E3S Web Conf.* **2025**, *601*, 00018. [CrossRef]
44. Yu, N.; Duan, W.; Fan, X. Hydrogen-fueled microgrid energy management: Novel EMS approach for efficiency and reliability. *Int. J. Hydrogen Energy* **2024**, *80*, 1466–1476. [CrossRef]
45. Guo, X.; Gu, F.; Liu, H.; Yu, Y.; Li, R.; Wang, J. Sustainable PV-hydrogen-storage microgrid energy management using a hierarchical economic model predictive control framework. *Energy Inform.* **2025**, *8*, 18. [CrossRef]
46. Qi, N.; Huang, K.; Fan, Z.; Xu, B. Long-term energy management for microgrid with hybrid hydrogen-battery energy storage: A prediction-free coordinated optimization framework. *Appl. Energy* **2025**, *377*, 124485. [CrossRef]
47. Zheng, Y.; Jia, J.; An, D. Energy Management for Microgrids with Hybrid Hydrogen-Battery Storage: A Reinforcement Learning Framework Integrated Multi-Objective Dynamic Regulation. *Processes* **2025**, *13*, 2558. [CrossRef]
48. Tang, Y.; Xun, Q.; Liserre, M.; Yang, H. Energy management of electric-hydrogen hybrid energy storage systems in photovoltaic microgrids. *Int. J. Hydrogen Energy* **2024**, *80*, 1–10. [CrossRef]
49. Alsolami, M.; Alferidi, A. Real-Time Energy Management of a Microgrid Using MPC-DDQN-Controlled V2H and H2V Operations with Renewable Energy Integration. *Energies* **2025**, *18*, 4622. [CrossRef]
50. Kang, J.; Fang, H.; Yun, L. A control and power management scheme for photovoltaic/fuel cell/hybrid energy storage DC microgrid. In Proceedings of the 2019 14th IEEE Conference on Industrial Electronics and Applications (ICIEA), Xi'an, China, 19–21 June 2019; pp. 1937–1941. [CrossRef]
51. Sahri, Y.; Belkhier, Y.; Tamalouzt, S.; Ullah, N.; Shaw, R.N.; Chowdhury, M.S.; Techato, K. Energy management system for hybrid PV/wind/battery/fuel cell in microgrid-based hydrogen and economical hybrid battery/super capacitor energy storage. *Energies* **2021**, *14*, 5722. [CrossRef]
52. Zhou, S.; Zhang, X.; Luo, Y.; Zhang, Y.; Lu, Y. The dynamic power sharing method for hydrogen-battery-supercapacitor hybrid energy storage system in DC microgrid. *J. Phys. Conf. Ser.* **2024**, *2918*, 012024. [CrossRef]
53. Nair, U.R.; Costa-Castello, R. A Model Predictive Control-Based Energy Management Scheme for Hybrid Storage System in Islanded Microgrids. *IEEE Access* **2020**, *8*, 97809–97822. [CrossRef]
54. Jia, C.; Cui, J.; Qiao, W.; Qu, L. Real-Time Model Predictive Control for Battery-Supercapacitor Hybrid Energy Storage Systems Using Linear Parameter-Varying Models. *IEEE J. Emerg. Sel. Top. Power Electron.* **2023**, *11*, 251–263. [CrossRef]
55. Deng, Z.; Chen, Q.; Zhang, L.; Zong, Y.; Zhou, K.; Fu, Z. Control oriented data driven linear parameter varying model for proton exchange membrane fuel cell systems. *Appl. Energy* **2020**, *277*, 115540. [CrossRef]

56. Vivas Fernández, F.J.; Manzano, F.S.; Márquez, J.M.A.; Calderón Godoy, A.J. Extended model predictive controller to develop energy management systems in renewable source-based smart microgrids with hydrogen as backup. Theoretical foundation and case study. *Sustainability* **2020**, *12*, 8969. [CrossRef]
57. Wang, R.; Zhou, X.; Wang, Y.; Xiao, Y.; Shi, Z.; Liu, Y.; Zhang, T. Degradation analysis of lithium-ion batteries under ultrahigh-rate discharge profile. *Appl. Energy* **2024**, *376*, 124241. [CrossRef]
58. Schmitt, J.; Rehm, M.; Karger, A.; Jossen, A. Capacity and degradation mode estimation for lithium-ion batteries based on partial charging curves at different current rates. *J. Energy Storage* **2023**, *59*, 106517. [CrossRef]
59. Peresada, S.; Nikonenko, Y.; Kovbasa, S.; Kuznietsov, A.; Pushnitsyn, D. Rapid Prototyping Station for Batteries-Supercapacitors Hybrid Energy Storage Systems. In Proceedings of the 2019 IEEE 39th International Conference on Electronics and Nanotechnology (ELNANO), Kyiv, Ukraine, 16–18 April 2019; pp. 826–831. [CrossRef]
60. Tekin, M.; Karamangil, M.İ. Comparative analysis of equivalent circuit battery models for electric vehicle battery management systems. *J. Energy Storage* **2024**, *86*, 111327. [CrossRef]
61. Lavety, S.; Keshri, R.K.; Chaudhari, M.A. A dynamic battery model and parameter extraction for discharge behavior of a valve regulated lead-acid battery. *J. Energy Storage* **2021**, *33*, 102031. [CrossRef]
62. Kujundžić, G.; Ileš, Š.; Matuško, J.; Vašak, M. Optimal charging of valve-regulated lead-acid batteries based on model predictive control. *Appl. Energy* **2017**, *187*, 189–202. [CrossRef]
63. Baccouche, I.; Jemmali, S.; Manai, B.; Omar, N.; Essoukri Ben Amara, N. Improved OCV model of a Li-ion NMC battery for online SOC estimation using the extended Kalman filter. *Energies* **2017**, *10*, 764. [CrossRef]
64. Vivas, F.J.; Segura, F.; Andújar, J.M.; Caparrós, J.J. A suitable state-space model for renewable source-based microgrids with hydrogen as backup for the design of energy management systems. *Energy Convers. Manag.* **2020**, *219*, 113053. [CrossRef]
65. Nemes, R.; Ciornei, S.; Ruba, M.; Hedesiu, H.; Martis, C. Modeling and simulation of first-order Li-Ion battery cell with experimental validation. In Proceedings of the 2019 8th International Conference on Modern Power Systems (MPS), Cluj-Napoca, Cluj, Romania, 21–23 May 2019. [CrossRef]
66. Andújar, J.M.; Barragán, A.J.; Vivas, F.J.; Enrique, J.M.; Segura, F. Iterative Nonlinear Fuzzy Modeling of Lithium-Ion Batteries. *Batteries* **2023**, *9*, 100. [CrossRef]
67. Yang, S.; Zhou, S.; Hua, Y.; Zhou, X.; Liu, X.; Pan, Y.; Ling, H.; Wu, B. A parameter adaptive method for state of charge estimation of lithium-ion batteries with an improved extended Kalman filter. *Sci. Rep.* **2021**, *11*, 5805. [CrossRef]
68. Samal, K.B.; Pati, S.; Sharma, R. A review of FCs integration with microgrid and their control strategies. *Int. J. Hydrogen Energy* **2023**, *48*, 35661–35684. [CrossRef]
69. Hossain, M.B.; Islam, M.R.; Muttaqi, K.M.; Sutanto, D.; Agalgaonkar, A.P. Modeling and performance analysis of renewable hydrogen energy hub connected to an ac/dc hybrid microgrid. *Int. J. Hydrogen Energy* **2022**, *47*, 28626–28644. [CrossRef]
70. Andújar, J.M.; Segura, F.; Rey, J.; Vivas, F.J. Batteries and Hydrogen Storage: Technical Analysis and Commercial Revision to Select the Best Option. *Energies* **2022**, *15*, 6196. [CrossRef]
71. Vivas, F.J.; Segura, F.; Andújar, J.M.; Palacio, A.; Saenz, J.L.; Isorna, F.; López, E. Multi-objective fuzzy logic-based energy management system for microgrids with battery and hydrogen energy storage system. *Electronics* **2020**, *9*, 1074. [CrossRef]
72. Vivas, F.J.; De las Heras, A.; Segura, F.; Andújar, J.M. H2RES2 simulator. A new solution for hydrogen hybridization with renewable energy sources-based systems. *Int. J. Hydrogen Energy* **2017**, *42*, 13510–13531. [CrossRef]
73. Ursúa, A.; Sanchis, P. Static-dynamic modelling of the electrical behaviour of a commercial advanced alkaline water electrolyser. *Int. J. Hydrogen Energy* **2012**, *37*, 18598–18614. [CrossRef]

Disclaimer/Publisher's Note: The statements, opinions and data contained in all publications are solely those of the individual author(s) and contributor(s) and not of MDPI and/or the editor(s). MDPI and/or the editor(s) disclaim responsibility for any injury to people or property resulting from any ideas, methods, instructions or products referred to in the content.